



## Article

# Numerical Simulation Study on the Influence of Twist Tape Parameters on Hydrate Particle Deposition

Shuli Wang<sup>1</sup>, Yongchao Rao<sup>2,3,\*</sup> , Chengming Hao<sup>1</sup>, Jing Yao<sup>1</sup> and Shidong Zhou<sup>2,3</sup> 

<sup>1</sup> School of Energy, Quanzhou Vocational and Technical University, Quanzhou 362268, China; wsl@cczu.edu.cn (S.W.); w18695665035@163.com (C.H.); w1065070275@163.com (J.Y.)

<sup>2</sup> School of Petroleum and Gas Engineering, Changzhou University, Changzhou 213164, China; zsd@cczu.edu.cn

<sup>3</sup> School of Energy, Changzhou University, Changzhou 213164, China

\* Correspondence: ryc@cczu.edu.cn; Tel.: +86-15961296997

**Abstract:** Numerical simulation is used to carry out research on the swirl flow transportation of a hydrate in the pipeline under the condition of the whole rotation of the twist tape using DPM (discrete phase modeling) and RNG (renormalization group)  $k-\epsilon$ . The influence of different twist tape parameters on the swirl number and concentration distribution of hydrate particles is analyzed. The structure parameters of the twist tape are optimized, based on the swirl efficiency evaluation parameters of a gas-solid two-phase pipeline. Finally, the twist tape is compared with different working conditions: the local rotation of twist tape and an ordinary pipeline. The results show that the areas of a high concentration of particles are near the twist tapes, and the concentration of particles on the leeward side of the twist tapes is higher than that on the windward side. The minimum concentration area at the axial position gradually increases with the increase of the flow distance, and the hydrate particles do not deposit at the bottom of the whole pipe section. The placement angle of the twist tape is greater, and the particle concentration area near the twist tape is also larger. The best placement angle is  $25^\circ$ . Under the condition of constant swirl strength, the range of the high particle concentration area will not increase indefinitely, and it is constant when the height of the twist tape is  $D/6$  and the optimal height is  $D/6$ . There should not be too many twist tapes, as this will affect the carrying effect. The optimal number of twist tapes is three. The particle carrying distance of the local swirl flow generation is about double that of the ordinary pipe. The particle carrying distance of the four twist tape pipes is 3.5 times greater than that of the ordinary pipe. The particle carrying distance of the whole swirl flow generation is 6.6 times higher than that of the ordinary pipe. The particle carrying effect is 89% higher than that of the four twist tape pipes. The particle carrying effect is 230% higher than that of the local swirl flow generation. The particle carrying effect is 560% higher than that of the ordinary pipe.

**Keywords:** swirl flow; twist tape; deposition; numerical simulation



**Citation:** Wang, S.; Rao, Y.; Hao, C.; Yao, J.; Zhou, S. Numerical Simulation Study on the Influence of Twist Tape Parameters on Hydrate Particle Deposition. *Processes* **2023**, *11*, 1658. <https://doi.org/10.3390/pr11061658>

Academic Editor:

Enrique Rosales-Asensio

Received: 27 April 2023

Revised: 18 May 2023

Accepted: 20 May 2023

Published: 29 May 2023



**Copyright:** © 2023 by the authors. Licensee MDPI, Basel, Switzerland. This article is an open access article distributed under the terms and conditions of the Creative Commons Attribution (CC BY) license (<https://creativecommons.org/licenses/by/4.0/>).

## 1. Introduction

Pipeline transportation has always been the most important mode of oil and gas transportation [1]. Its advantages are low cost, large transportation volume, high efficiency, and great stability. The nature of the safety risk in oil and gas pipeline accidents involves great harm and significant damage [2]. Moreover, the oil and gas pipeline operation runs under pressure, works continuously, and covers a significant area and a diversified environment. Once the pipeline is blocked and leaks, there will be very significant consequences [3].

Gudmundsson et al. [4–6] put forward Hydraflow technology and the cold flow concept, the core idea of which is to allow or guide the formation of natural gas hydrate in the pipeline and to keep the form of tiny grains flowing evenly and steadily along with the fluid so as to avoid accidents in a gas transmission pipeline from hydrate accumulation

and blockage and to ensure the safe flow of gas in the transmission pipeline. Wang's research group [7,8] put forward the swirl flow hydrate control technology based on the flow characteristics of swirl flow to ensure the safe flow of hydrate slurry. This technology has two advantages: (1) because the swirl flow can increase the shear stress of fluid, it is difficult for hydrate particles to deposit and bond on the pipe wall, thus increasing the transportation distance of the hydrate particles; (2) because the swirl flow can enhance the speed of hydrate particles and the liquid bridge force between particles is destroyed, the deposition of the hydrate particles is greatly reduced [9].

For a numerical simulation study, Zhou et al. [10] investigated the effect of swirl diameter and swirl angle on flow conversion using the CLSVOF (coupled level-set and volume of fluid) method. Wang et al. [11] studied the gas–liquid two-phase swirl flow pattern transformation law. The swirl generation used was the impeller. The author analyzed the effect of different impeller areas and the angle convection on the flow pattern. Dai et al. [12] investigated the gas–liquid two-phase swirl flow pattern in a horizontal pipe. The liquid phase involved the addition of SDBS (sodium dodecyl benzene sulfonate). It was found that SDBS can change the conversion boundary of the swirl annular flow. Cai et al. [13] studied the flow pattern map. The author compared this with the vertical pipeline flow pattern and found that the swirl annular flow region increases when the intermittent flow region decreases. Liu et al. [14] studied the flow characteristics of the slug flow in a horizontal pipe. The pipe was a rectangular-section swirl channel. Liu et al. [15] investigated the gas–liquid two-phase flow pattern using the RSM and VOF models. It was found that bubble flow, stratified flow, wavy flow, slug flow, and annular flow can be simulated.

For an experimental study, Cui et al. [16] used R134a as the working fluid to experimentally study the boiling gas–liquid two-phase flow pattern and pressure drop characteristics in the microfin swirl coil and obtained the layered wave flow, intermittent flow, and annular flow. With the steam flow as the abscissa and the mass flow of the two phases as the ordinate, the flow pattern map is obtained. Subhashini and Nigam [17] studied the effect of the gas-bearing rate on the flow pattern in swirl flow heat exchangers. The experiment obtained the stratified flow, the slug flow, the plug flow, the wave flow, and the agitation flow. Liu et al. [18] used high-speed flow visualization to experimentally study the gas–water two-phase flow characteristics in a vertical swirl rectangular channel. The flow pattern map of the swirl rectangular channel was obtained, and the evolution process of the flow pattern at different positions of the swirl rectangular channel was expounded. Fabio and Gerhardt [19] studied the gas–liquid two-phase flow with twist tape and obtained a total of five types of flow patterns: stratified flow, intermittent flow, annular stratified flow, annular flow, and plug flow. Wang et al. [20] studied the swirl flow characteristics in surfactant systems. The effects of flow pattern, gas content, vane parameters, surfactant concentration, and the flow rate on pressure drop were systematically investigated. Wang et al. [21–24] also conducted exploratory research on gas–liquid two-phase flow patterns and studied the flow pattern and flow pattern transition boundary of a gaslit-aided two-phase swirl flow with a vane and twisted type. Liu et al. [25,26] investigated the axial development of air–water annular flow with swirl in a vertical pipe. Liu et al. [27] studied the characteristics of single-phase and gas–liquid two-phase swirl flows induced by short swirl ties. It was found that the pitch of the swirl vortex decreases with the increase of the Reynolds number in a single-phase flow, the axial velocity of the gas phase appears as two peaks in a gas–liquid two-phase annular mist flow, and the distribution of the liquid phase is uneven along the circumference. Cai et al. [28] studied the flow characteristics of hydrate slurry in the long-twisted zone via numerical simulation and found that the vorticity had no attenuation and increased with the decrease of the twist rate. The volume fraction of hydrate particles is symmetrically distributed around the twisted band. Wang et al. [29,30] carried out a comparative analysis of the effects of impellers with different sizes and rotation angles on the gas–liquid two-phase flow and classified the flow patterns into six types. It was found that the flow pattern had the greatest influence on the pressure drop. Liang et al. [31]

numerically simulated the gas–solid two-phase helical flow characteristics and heat transfer law in a horizontal tube with twist tape. It was found that swirl flow particles have strong carrying capacity, which can strengthen heat transfer among hydrate particles and prevent safety accidents caused by hydrate blockage in natural gas pipelines. Hu et al. [32] set up a pipeline test system and made a multi-guide vane local rotating device to study the effect of polyacrylamide (PAM) on the flow characteristics of pipeline swirl flow. It was found that after adding a small amount of PAM (100 mg/L), the velocity distribution of pipeline swirl flow was 67% longer than that of clean water, and the solid conveying capacity of pipeline swirl flow increased by 79.1%~91.5%.

However, at present, the research on swirl flow in pipelines mostly uses local twist tape, such as short twist tape [33] and impellers [34], to generate swirl flow [35,36], which attenuates quickly; therefore, many relays need to be installed for long-distance pipeline applications. There is little research on the entire twist process. Therefore, in this paper, the swirl flow is generated by the complete rotation of the twist tape, and the influence of the twist tape parameters on the deposition characteristics of hydrate particles is studied, which provides theoretical basis and technical guidance for the safe transportation of natural gas hydrate by swirl flow.

## 2. Numerical Simulation Method

### 2.1. Physical Model

#### 2.1.1. Geometric Model

Because the formation of natural gas hydrate needs to pass through a series of complex physical and chemical processes, it does not exist directly in the pipeline. In this paper, only the flow of hydrate is studied in the numerical simulation process, and the formation of hydrate in the flow process is ignored, so it is assumed that hydrate particles have been formed at the entrance of the pipeline. In numerical simulation, the shape of hydrate particles is assumed to be a regular sphere with the same particle size, and the influence of the wall thickness of the pipeline system on hydrate formation is ignored in numerical simulation. The geometric model of diversion is shown in Figure 1. The horizontal pipe has a diameter of  $D = 0.032$  m and a length of  $L = 2$  m, and a twist tape is installed from the entrance. The numerical simulation calculation adopts the X-Y-Z three-dimensional rectangular coordinate system; the origin of the coordinate is set as the center of the entrance face of the pipeline, and the flow direction is set as the positive direction of the Z-axis, flowing from the left end to the right end of the pipeline.

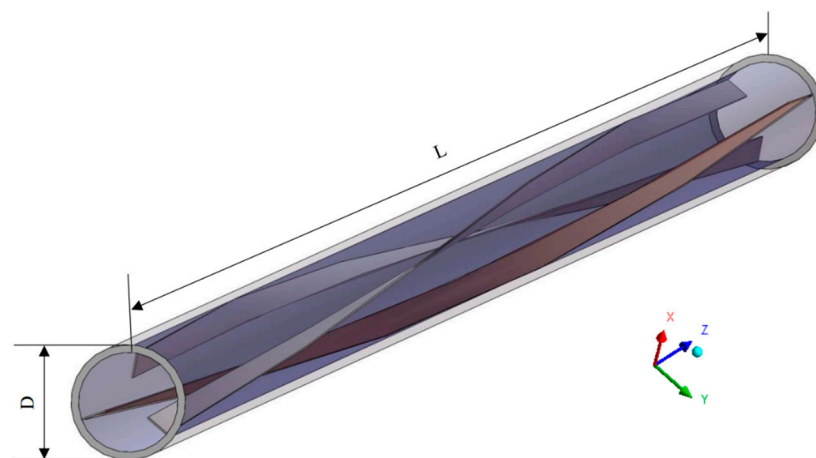


**Figure 1.** Geometric model.

#### 2.1.2. Boundary Conditions

Velocity-inlet is used as the boundary condition at the inlet of the pipeline, and Reynolds numbers of 5000 and 20,000 are used as the velocity inlet conditions. The outlet

boundary condition is set to outflow, and the wall boundary condition is set to a fixed non-slip wall. The gravity direction is along the Y direction, and the acceleration of gravity is  $9.81 \text{ m/s}^2$ .

### 2.1.3. Initial Conditions

The continuous phase fluid is natural gas, and the discrete phase is natural gas hydrate particles, and their basic physical parameters are measured at 277 K. The natural gas density is  $0.77 \text{ kg/m}^3$ , and the dynamic viscosity is  $1.1035 \times 10^{-5} \text{ Pa}\cdot\text{s}$ . The particle density of hydrate is  $915 \text{ kg/m}^3$ . In the simulation, data parameters are selected according to the specific research content.

### 2.2. Grid Division

ICEM-CFD software is used to mesh the three-dimensional geometric model. The entire pipe adopts unstructured mesh, and the edge and wall mesh of the twist tape are encrypted. The thickness of the bottom layer is 0.2 mm, and 5 layers are encrypted according to the ratio of 1.1. The line grid is set at the intersection of the diversion channel and the wall, and the maximum size is 0.5 mm. Grid division results are shown in Figure 2.

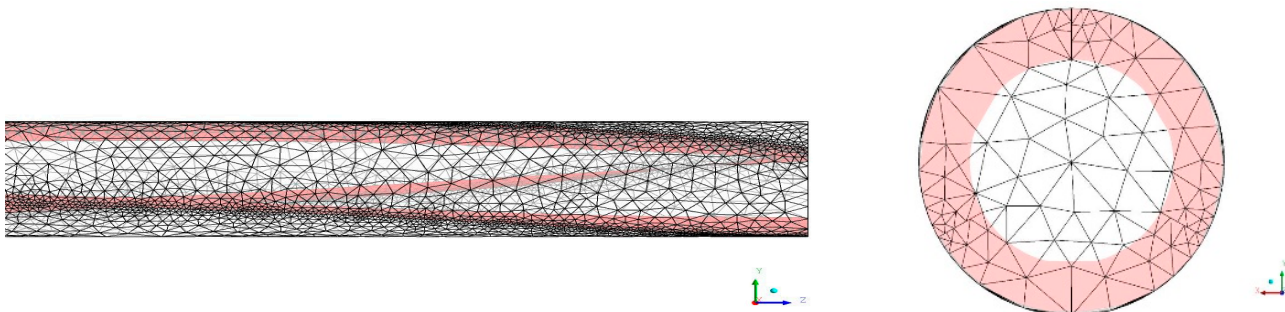


**Figure 2.** Mesh division.

### 2.3. Mathematical Model

The gas–solid two-phase flow simulation adopts the DPM (discrete phase model), which is a multicomponent flow model based on the Euler–Lagrange method. In the simulation calculation, the solid particles are regarded as discrete phase, while the fluid is regarded as continuous phase. In the calculation, the continuous phase of the fluid is calculated first, and the discrete phase added with particles is calculated again after it is stable.

#### 2.3.1. Control Equation

The continuity equation is [37]

$$\frac{\partial \rho}{\partial t} + \nabla(\rho v) = 0 \quad (1)$$

The momentum equation is

$$\begin{cases} \frac{\partial(\rho u)}{\partial t} + \text{div}(\rho u \vec{w}) = \frac{\partial \tau_{xx}}{\partial x} + \frac{\partial \tau_{yx}}{\partial y} + \frac{\partial \tau_{zx}}{\partial z} - \frac{\partial p}{\partial x} + F_x \\ \frac{\partial(\rho v)}{\partial t} + \text{div}(\rho v \vec{w}) = \frac{\partial \tau_{xy}}{\partial x} + \frac{\partial \tau_{yy}}{\partial y} + \frac{\partial \tau_{zy}}{\partial z} - \frac{\partial p}{\partial y} + F_y \\ \frac{\partial(\rho w)}{\partial t} + \text{div}(\rho w \vec{w}) = \frac{\partial \tau_{xz}}{\partial x} + \frac{\partial \tau_{yz}}{\partial y} + \frac{\partial \tau_{zz}}{\partial z} - \frac{\partial p}{\partial z} + F_z \end{cases} \quad (2)$$

where  $\rho$  is the gas density,  $\text{kg/m}^3$ ;  $u$ ,  $v$  and  $w$  are all velocities,  $\text{m/s}$ ;  $P$  is static pressure,  $\text{Pa}$ ;  $\tau_{ij}$  is the viscous stress tensor, and  $t$  is time,  $\text{s}$ .



### 2.3.2. Turbulent Motion Equation

Gas–solid simulation adopts the RNG k- $\varepsilon$  turbulence model because it is suitable for complex shear flow with strong swirl. The transmission equation model of turbulence kinetic energy and dissipation rate  $\varepsilon$  is

$$\frac{\partial}{\partial t}(\rho k) + \frac{\partial}{\partial x_j}(\rho k u_j) = \frac{\partial}{\partial x_j} \left( \left( \mu + \frac{\mu_t}{\sigma_k} \right) \frac{\partial k}{\partial x_j} \right) + G_k + G_b - \rho \varepsilon \quad (3)$$

$$\frac{\partial}{\partial t}(\rho \varepsilon) + \frac{\partial}{\partial x_j}(\rho \varepsilon u_j) = \frac{\partial}{\partial x_j} \left( \left( \mu + \frac{\mu_t}{\sigma_\varepsilon} \right) \frac{\partial \varepsilon}{\partial x_j} \right) + \rho C_{1\varepsilon} S \varepsilon - \rho C_{2\varepsilon} \frac{\varepsilon^2}{k + \sqrt{v \varepsilon}} + C_{1\varepsilon} \frac{\varepsilon}{k} G_b \quad (4)$$

Among:

$$C_1 = \max \left[ 0.43, \frac{\eta}{\eta + 5} \right], \eta = S \frac{k}{\varepsilon}, S = \sqrt{2 S_{ij} S_{ij}}, S_{ij} = \frac{1}{2} \left( \frac{\partial u_j}{\partial x_i} + \frac{\partial u_i}{\partial x_j} \right), \mu_t = \rho C_\mu \frac{k^2}{\varepsilon} \quad (5)$$

where type  $\rho$  is the gas density, kg/m<sup>3</sup>;  $G_k$  and  $G_b$  represent turbulence kinetic energy due to average velocity gradient and buoyancy;  $C_{1\varepsilon}$  and  $C_{2\varepsilon}$  are turbulence model coefficients, with  $C_{1\varepsilon} = 1.42$  and  $C_{2\varepsilon} = 1.68$ ;  $\sigma_k$  and  $\sigma_\varepsilon$  are the turbulent Prandtl numbers of  $k$  and  $\varepsilon$ ,  $\sigma_k = \sigma_\varepsilon = 1.39$ ;  $u$  and  $v$  are both velocities, m/s, and  $C_\mu = 0.0845$ .

### 2.3.3. Discrete Phase Model Equation

The DPM obtains the particle motion equation by calculating the force exerted on the particle, and the particle motion trajectory can be obtained by integrating the particle motion equation of the DPM with time. Its motion trajectory equation is

$$\frac{d u_p}{d t} = F_D(u - u_p) + \frac{g_z(\rho_p - \rho)}{\rho_p} + F_Z \quad (6)$$

where  $u$  is the fluid phase velocity, m/s;  $u_p$  is the particle velocity, m/s;  $g_z$  is the component of gravitational acceleration in  $z$  direction, m/s<sup>2</sup>;  $\rho$  is the fluid density, kg/m<sup>3</sup>;  $\rho_p$  is the particle density, kg/m<sup>3</sup>, and  $F_z$  is the other forces on the particles (such as Brownian force, additional mass force, Saffman lift force, etc.). The additional mass force only works when the fluid density is greater than the particle density, so the additional mass force is not considered because the particle density of hydrate in the pipe is much greater than that of natural gas. Because there will be a velocity difference perpendicular to the movement direction of particles when flowing, the Saffman lift force will be generated, so it is necessary to consider the Saffman lift force.

Among them,  $F_D$  is defined as:

$$F_D = \frac{18\mu}{\rho_p d_p^2} \frac{C_D Re}{24} \quad (7)$$

Re is the relative Reynolds number, and its definition formula is as follows:

$$Re = \frac{\rho d_p |u_p - u|}{\mu} \quad (8)$$

Type,  $d_p$  is the particle diameter, m.

The drag coefficient  $C_D$  can be expressed as follows:

$$C_D = a_1 + \frac{a_2}{Re} + \frac{a_3}{Re} \quad (9)$$

As the simulated Re value is 20,000, the values of  $A_1$ ,  $A_2$ , and  $A_3$  are 0.5191,  $-16,625.5$ , and 5,416,700, respectively.

#### 2.4. Calculation Method

With the popularization and performance improvement of computers and the development of computational fluid dynamics, it is possible to investigate flow characteristics by using numerical simulation technology after some reasonable simplification of engineering problems. Compared with theoretical analysis and the calculation method, numerical simulation technology can better meet the needs of complex engineering problems. Numerical simulation usually uses CFD software to solve practical problems. The software generally consists of three parts: pre-processing, data calculation, and post-processing. Pre-processing is carried out to establish a physical model and then mesh, and the middle part of the calculation is particularly important. Before operation, many parameters and algorithm choices need to be set, among which the selection of algorithm can improve the accuracy of simulation and calculation efficiency. Post-processing is carried out using CFD-Post, Tecplot, Origin, and other post-processing software to analyze the calculated data file to describe the calculated data intuitively.

In the calculation, the discrete phase model is selected, and the pressure-based implicit solver is used for three-dimensional transient simulation [35,36]. When simulating the discrete phase, the DPM is used as the particle motion model; the RNG  $k-\epsilon$  model is used as the turbulence model; the SIMPLEC algorithm is used to calculate the pressure and velocity, and the second-order format is used for the pressure. The particle velocity, mass flow rate, and particle concentration are set at the inlet of the pipeline. In order to obtain better calculation results,  $\epsilon_p = 0.3\sim 0.7$ ,  $\epsilon^{-6} = 0.5\sim 0.7$ ,  $\epsilon_k = \epsilon_\epsilon = 0.4\sim 0.6$ , and the absolute value of calculation residual is defined as  $< 1 \times 10^{-6}$ .

Through the data obtained from the previous three-dimensional transient calculation, you can observe some cloud images depicting pressure, velocity, and temperature in Fluent to see the difference with the theoretical effect, or you can import the data into Tecplot post-processing software to process the simulated content in detail.

#### 2.5. Grid independence Verification

To reduce the influence of the number of grids on the calculation results and improve the efficiency of simulation, grid independence verification is used to screen the number of grids. The grids with the number of grids ranging from  $2 \times 10^5$  to  $2 \times 10^6$  are selected for simulation under the same initial and boundary conditions. Compare the effects of different grid numbers on the average axial velocity and tangential velocity in the tube, and the results are shown in Figure 3. Through comparative analysis, it can be found that when the number of grids is greater than  $8 \times 10^5$ , the tangential velocity and axial velocity are less affected by the number of grids. Therefore, a grid with a grid number of about  $1 \times 10^6$  is selected to ensure both high computational efficiency and high accuracy of results.

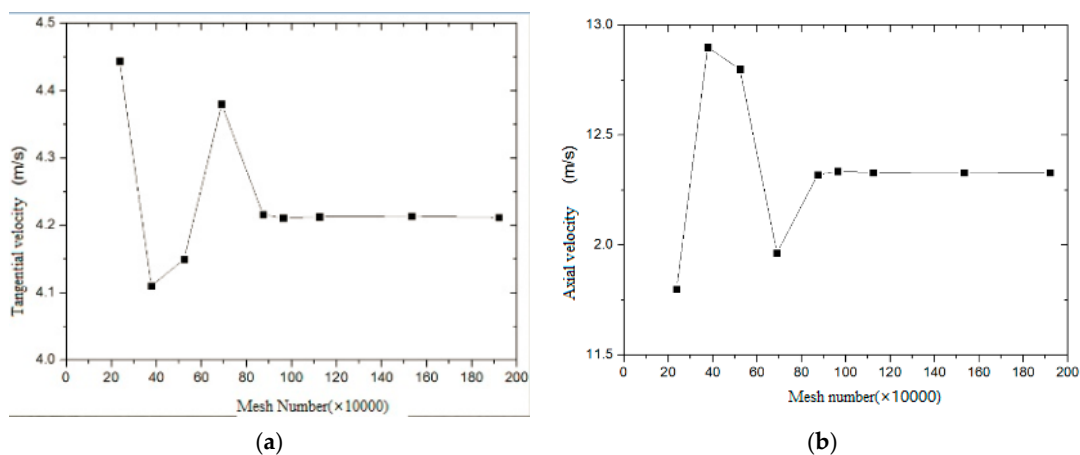


**Figure 3.** Grid independence verification. (a) Graph of tangential velocity changing with grid. (b) Diagram of axial velocity changing with grid.

## 2.6. Model Feasibility Verification

Zhou Jiawei [37] studied the influence of coal particle size on the critical pick-up speed in the swirl flow system by using the twist tape as the starting device and a self-improved experimental device for measuring the critical speed of coal particles. Comparing Zhou's experimental results with the simulation results (as shown in Figure 4), the feasibility of this model can be verified to some extent. From the comparison between Zhou's experiment and simulation results, it is found that the solid phase in Zhou's experiment is coal particles, and there is a certain error between the results and the simulation results in this paper. The tangential velocity simulation results are slightly larger than Zhou's experimental results, but the overall error is small, and the asymmetric distribution of tangential velocity in numerical simulation in this paper is also consistent with the experimental results. The error between the axial velocity simulation results and the experimental results is very small and the data, especially the data at the axis, are basically consistent. Generally speaking, the whole process of gas–solid two-phase swirl flow with twist tape can be numerically simulated.

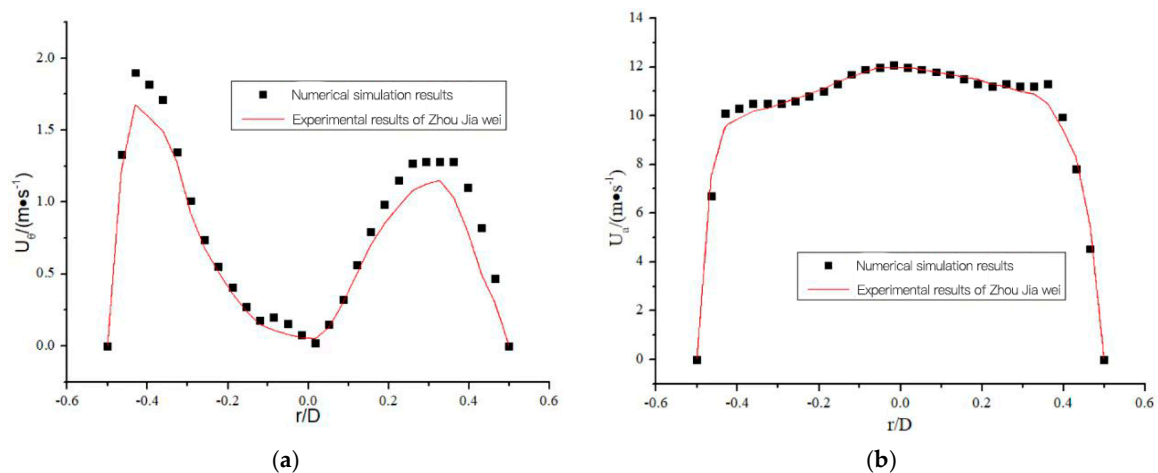


**Figure 4.** Comparison of numerical simulation and experimental results. (a) Comparison diagram of tangential velocity distribution along the diameter. (b) Comparison diagram of axial velocity distribution along the diameter.

## 3. Results and Discussion

### 3.1. Working Condition Setting

In this chapter, firstly, the influence of flow twist tape parameters on the hydrate particle settling law is studied and then compared with the influence of a local riser and common pipeline. A total of 24 groups are simulated. The operating parameters are shown in Table 1.

**Table 1.** Parameter table of simulated working conditions.

Working Condition	Initial Particle Concentration $\alpha_0/\%$	Particle Size $D_k/\mu\text{m}$	$Re$	Twist Tape Placement Angle $\theta$	Guide Height $h/\text{m}$	Number of Diversion Strips $n$	Twist Taping Mode
1	8	10	20,000	10°	D/6	3	Full rotation
2	8	10	20,000	15°	D/6	3	Full rotation
3	8	10	20,000	20°	D/6	3	Full rotation
4	8	10	20,000	25°	D/6	3	Full rotation
5	8	10	20,000	25°	D/5	3	Full rotation
6	8	10	20,000	25°	D/6	3	Full rotation
7	8	10	20,000	25°	D/8	3	Full rotation
8	8	10	20,000	25°	D/10	3	Full rotation
9	8	10	20,000	25°	D/6	3	Full rotation
10	8	10	20,000	25°	D/6	4	Full rotation

Table 1. Cont.

Working Condition	Initial Particle Concentration $\alpha_0/\%$	Particle Size $D_k/\mu\text{m}$	$Re$	Twist Tape Placement Angle $\theta$	Guide Height $h/\text{m}$	Number of Diversion Strips $n$	Twist Taping Mode
11	8	10	20,000	25°	D/6	6	Full rotation
12	8	10	20,000	25°	D/6	3	Full rotation
13	30	10	20,000	25°	D/6	3	Full rotation
14	40	10	20,000	25°	D/6	3	Full rotation
15	50	10	20,000	25°	D/6	3	Full rotation
16	10	10	5000	25°	D/6	3	Full rotation
17	12	10	5000	25°	D/6	3	Full rotation
18	14	10	5000	25°	D/6	3	Full rotation
19	16	10	5000	25°	D/6	3	Full rotation
20	18	10	5000	25°	D/6	3	Full rotation
21	20	10	5000	25°	D/6	3	Full rotation
22	10	10	5000	25°	D/6	3	Local rotation
23	10	10	5000		twist tape		Local rotation
24	10	10	5000		—		No rotation

### 3.2. Variation Law of Swirl Number

Swirl number  $s$  is a parameter representing the intensity of swirl flow, which is usually defined by the circumferential velocity or rotational angular velocity. The formula of swirl number  $s$  of swirl flow in a gas–solid two-phase pipeline is defined as follows:

$$S = \frac{\int_0^R u_\theta u_a r^2 dr}{R \int_0^R u_a^2 r dr} \quad (10)$$

where  $u_a$  is the axial speed, m/s;  $u_\theta$  is the tangential velocity, m/s;  $R$  is the pipe diameter, m;  $R$  is the radial coordinate of the swirl pipe, and the turbulence disturbance (pulsation) can be neglected; thus, the velocity is considered as the time average velocity.

Simplified:

$$S = \frac{2u_\theta}{3u_a} \quad (11)$$

As shown in Figure 5, there are two methods for obtaining radial swirl number. Method A is the data of the vertical section of the twist tape at the end of the first lead (close to the windward surface of the twist tape, but not the twist tape), and Method B is the data of the horizontal section of the twist tape at the end of the first lead.

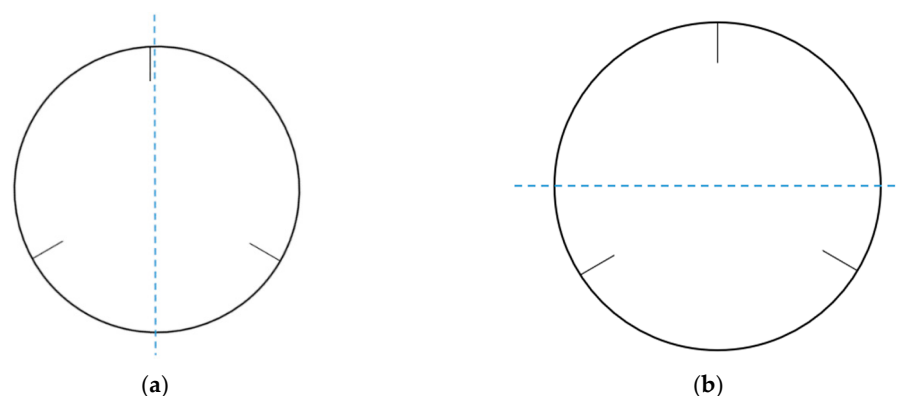
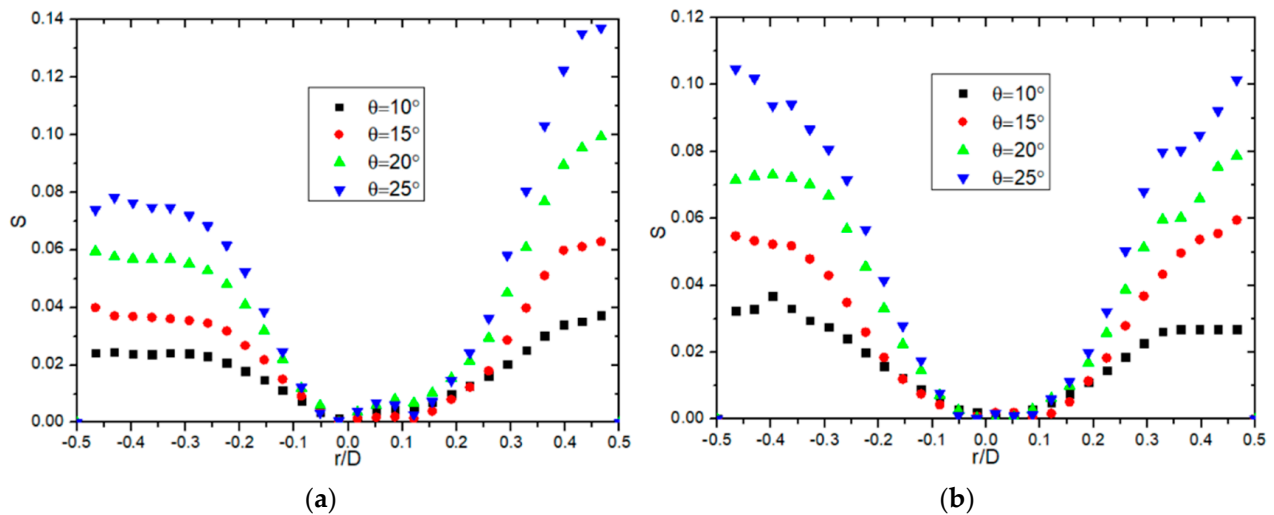


Figure 5. Schematic diagram of radial tangent line. (a) Vertical section. (b) Horizontal section.

#### 3.2.1. Influence of the Placing Angle of the Twist Tape on the Variation Law of swirl Number

As shown in Figure 6, the influence of the placement angle of the twist tape on the radial variation of swirl number under the condition of  $Re = 20,000$  is shown. It can be seen from the figure that the vertical radial swirl number is obviously higher on the side

that passes through the twist tape than on the side that does not pass through the twist tape, while the values on both sides of the horizontal radial swirl number are balanced. In addition to this difference, the overall value of radial swirl number increases with the increase of installation angle; its maximum value appears near the pipe wall, and the swirl number at the pipe axis tends toward zero.



**Figure 6.** Influence of the placement angle of twist tape on the radial variation of the swirl number. (a) Vertical section. (b) Horizontal section.

As shown in Figure 7, the influence of the placement angle of the twist tape on the variation of swirl number along the way under the condition of  $Re = 20,000$  is shown. It can be clearly seen from the figure that the swirl number of the twist tape is not constant all the time but is divided into two parts, namely, the acceleration section and the stable section. The curve of the stationary part of rotation is sinusoidal, and the larger the angle of the twist tape, the larger the deviation and amplitude of the curve, and the faster the fluctuation frequency. As can be seen from Figure 6, the larger the setting angle of the twist tape is, the larger the radial distribution value of the swirl number is, so the offset and amplitude of its sine function curve are also larger. As the lead of the 10-degree twist tape (the distance that the twist tape rotates 360 degrees along the pipe wall) is 1.069 m/r, that of the 15-degree twist tape is 0.703 m/r; that of the 20-degree twist tape is 0.517 m/r, and that of the 25-degree twist tape is 0.404 m/r, as can be seen from Figure 7. Figure 8 shows the circumferential variation of the swirl number of a pipeline with a twist tape setting angle of 25 degrees at a radius of  $0.4D$  under the working condition of  $Re = 20,000$ . It can be seen from the figure that the circumferential variation of the swirl number is periodic, and it is 120 degrees, rotationally symmetrical about the center of the circle. The swirl number is in the range from the windward side of the last twist tape to the leeward side of the next twist tape, and the swirl number first increases and then decreases. At the three positions of 30, 150, and 270 degrees (30 degrees from the windward side of the twist tape, respectively), it can be found that the number of swirling flows in the lower part of the pipeline is larger than that in the upper part. This is due to the conservation of energy, the mutual transformation of kinetic energy, and gravitational potential energy, and the number of swirling flow is converted by tangential velocity and axial velocity, so the number of swirling flow along the twist tape fluctuates sinusoidally.



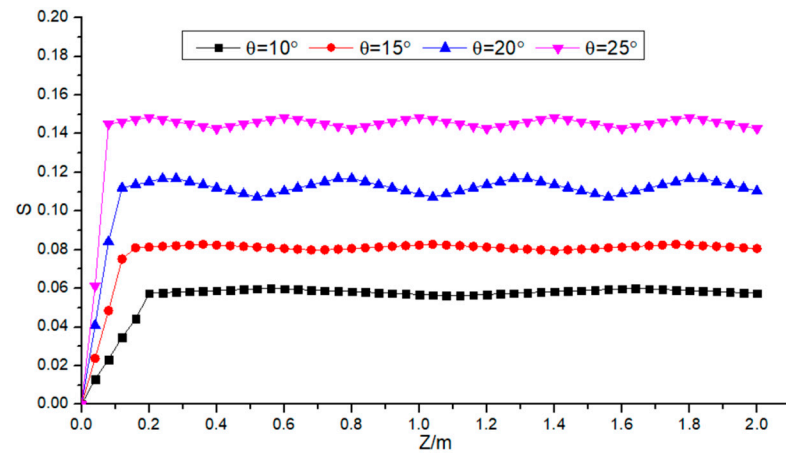


**Figure 7.** Influence of the placing angle of the twist tape on the variation of swirl number along the way.

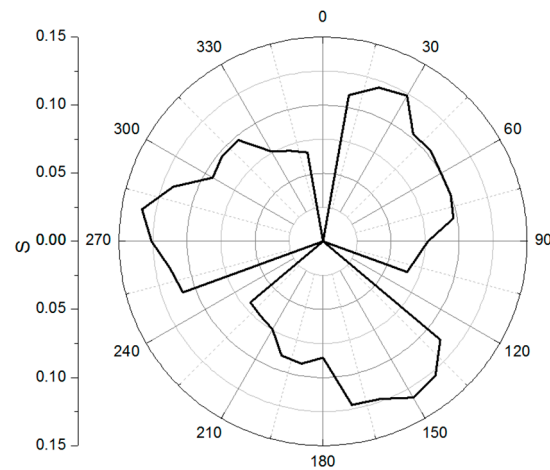


**Figure 8.** Circumferential change of swirl number of a twist tape pipe with the placement angle of  $25^\circ$  at a radius of  $0.4 D$ .

### 3.2.2. Influence of the Height of Twist Tape on the Variation Law of Swirl Number

As shown in Figure 9, the influence of the height of the twist tape on the radial variation of the swirl number under the condition of  $Re = 20,000$  is shown. The vertical radial swirl number on one side of the twist tape is obviously higher than that on the other side of the twist tape, while the values on both sides of the horizontal radial swirl number are balanced. In addition, the overall value of the radial swirl number increases with the height of the twist tape. The maximum value appears in the range of  $0.4\text{--}0.45 D$  and does not vary greatly; the swirl number at the axis of the pipeline approaches zero. This shows that the change of the height of the twist tape has little influence on the maximum value of the radial swirl number and has a great influence only on the existing range of strong swirl (the swirl number is greater than the half value of the swirl number on the same side). The higher the height of the twist tape, the larger the range of strong swirl. That is, the higher the height of the twist tape is, the slower the radial swirl number decays, and the maximum swirl number is basically unchanged. Figure 10 shows the influence of the height of the twist tape on the swirl number along the way under the condition of  $Re = 20,000$ . It can be found that the higher the height of the twist tape, the greater the swirl number along the way. In this part of the study, the height of the twist tape is the only variable, and the setting angle of the twist tape is fixed, so the fluctuation frequency of the curve is the same. However, when the height of the twist tape is  $D/10$ , the length of the rotating acceleration section in the curve is longer than that of the other 3 twist tape pipelines. This is because

the height of the twist tape is too short, and the twist tape cannot twist the main flow area at the axis well, so the twist tape effect is low. Therefore, when the height of the twist tape is  $D/10$ , the position of the initial swirl number in the curve is backward.

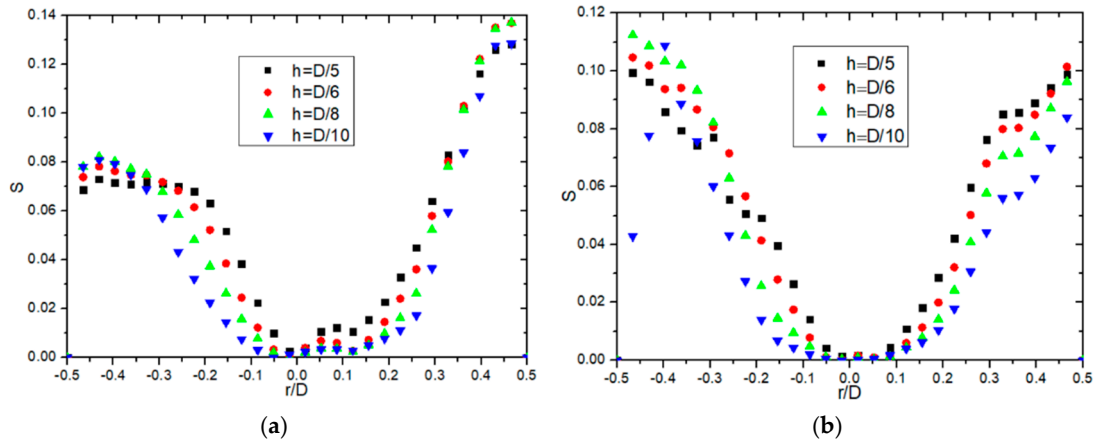


**Figure 9.** Influence of the height of the twist tape on the radial variation of the swirl number. (a) Vertical section. (b) Horizontal section.

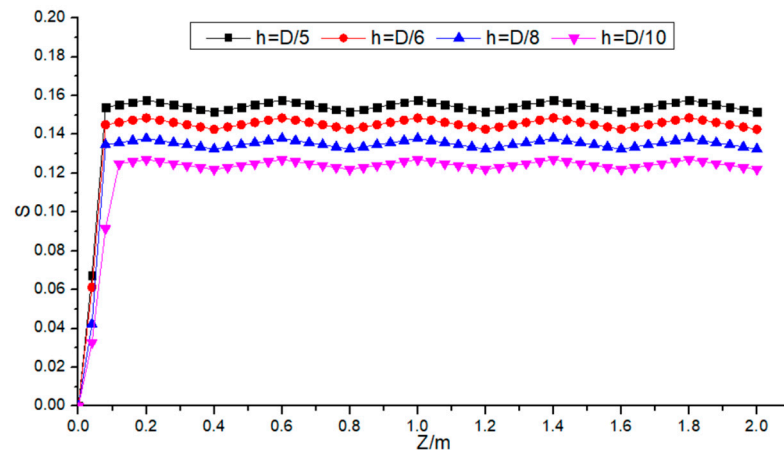


**Figure 10.** Influence of the height of twist tape on the variation of swirl number along the course.

### 3.2.3. Influence of the Number of Twist Tapes on the Variation Law of Swirl Number

Under the working condition of  $Re = 20,000$ , the circular point at the  $0.4 D$  circumference where the maximum swirl number appears is selected, and one point is selected every 10 degrees along the rotation direction. The point with 0 swirl number is the position of the twist tape. Since the height of the twist tape is greater than  $0.1 D$ , the selected point is located inside the twist tape, so the swirl number is 0. The value results are shown in Figure 11. From Figure 11, it can be found that the change of swirl number in the pipe is not symmetrical around the X-axis or Y-axis but rotationally symmetrical around the center of the circle at  $360/n$ , which shows a periodic change from the windward side of the twist tape to the leeward side of the next twist tape, which first increases and then decreases. The lower the number of twist tapes, the faster the number of swirling flows between the two plates decays. However, as shown in Figure 11, the number of swirls in the pipe with  $n = 6$  is too large; the distance between 2 flow guides is too short, and the effective flow area on the cross section is too low, resulting in the overall swirl number in the pipe being too low. Figure 12 shows the influence of the number of twist tapes on the swirl number along the way under the condition of  $Re = 20,000$ . It can be seen from the figure that the more twist tapes, the lower the swirl number along the way. In addition, in the curve of the swirl number along the way of the pipes with four and six twist tapes, the acceleration section of

the twist tape-off is obviously shorter than that of the pipes with three twist tapes. Because of the large number of twist tapes, the twist tape-off is faster.

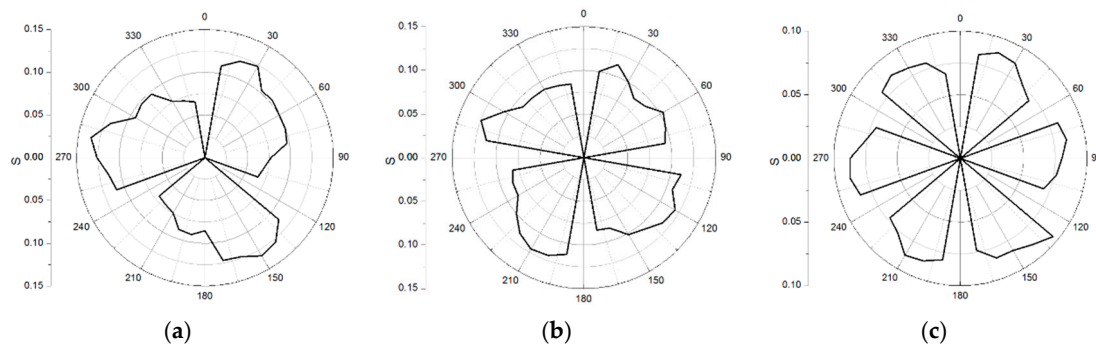


**Figure 11.** Influence of the number of twist tapes at the circumferential position at radius of 0.4 D on the change of the number of swirls. (a)  $n = 3$ . (b)  $n = 4$ . (c)  $n = 6$ .

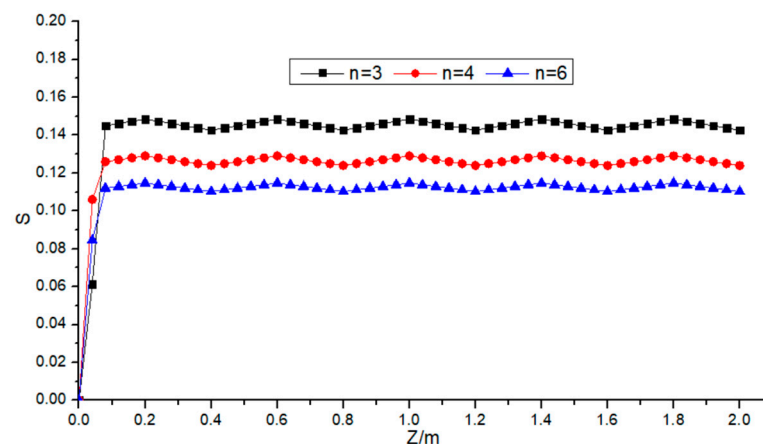


**Figure 12.** Influence of the number of twist tapes on the change of swirl number along the way.

### 3.3. Distribution Law of Particle Volume Fraction

#### 3.3.1. Influence of Placing Angle of Twist Tape on Particle Volume Fraction Distribution Law

Figures 13–15 show the relationship between the placement angle of the flow twist tape and the hydrate particle concentration in the pipe at the half-cycle or full-cycle cross section positions near the reference surfaces of  $Z = 10 D$ ,  $30 D$ , and  $50 D$  under the working condition of  $Re = 20,000$ . It can be seen from Figure 13 that the high-concentration areas of particles are concentrated near three twist tapes, the concentration of particles on the leeward side of the twist tape is higher than that on the windward side, and the minimum concentration area at the axis position gradually becomes larger with the increase of the flow distance. It shows that the swirl has a good particle carrying effect, and the particles will not be deposited in the center of the tube bottom due to the influence of gravity. At the setting angle, the concentration of particles on the windward side of the twist tape in the pipe with  $= 25$  degrees is higher than that in the other pipes with three different angles. At this time, the swirl flow is large, and the centrifugal force of the swirl flow on the particles is too large, so the particles are concentrated near the twist tape. However, due to the shear stress provided by the strong swirl flow, the hydrate particles will not deposit but will swirl forward close to the twist tape. Figure 16 shows the influence of the vertical tangent twist tape placement angle on the radial distribution of hydrate particle concentration at half-cycle or full-cycle positions near different reference surfaces under the working condition of  $Re = 20,000$ . The abscissa is the concentration, and the ordinate is the ratio of the distance between the detection point and the pipe axis and pipe diameter.

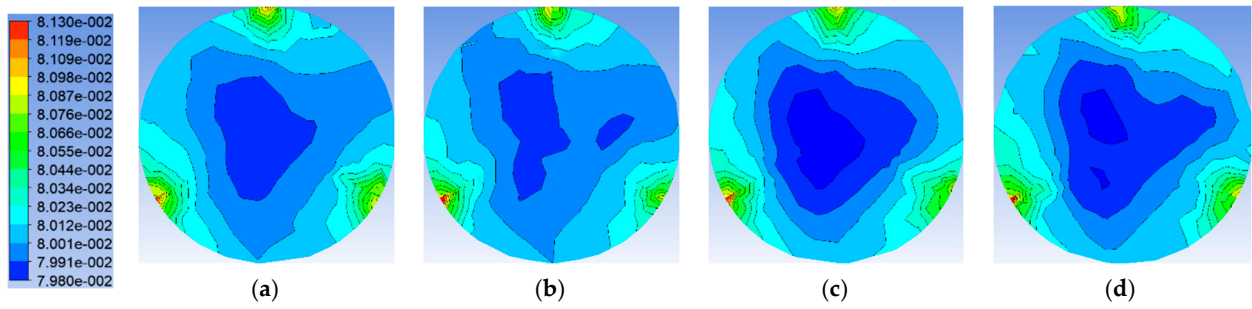


Figure 13. Influence of the placing angle of the twist tape near the reference plane of  $9 z = 10 d$  on the concentration distribution of hydrate particles. (a)  $\theta = 10^\circ$ . (b)  $\theta = 15^\circ$ . (c)  $\theta = 20^\circ$ . (d)  $\theta = 25^\circ$ .

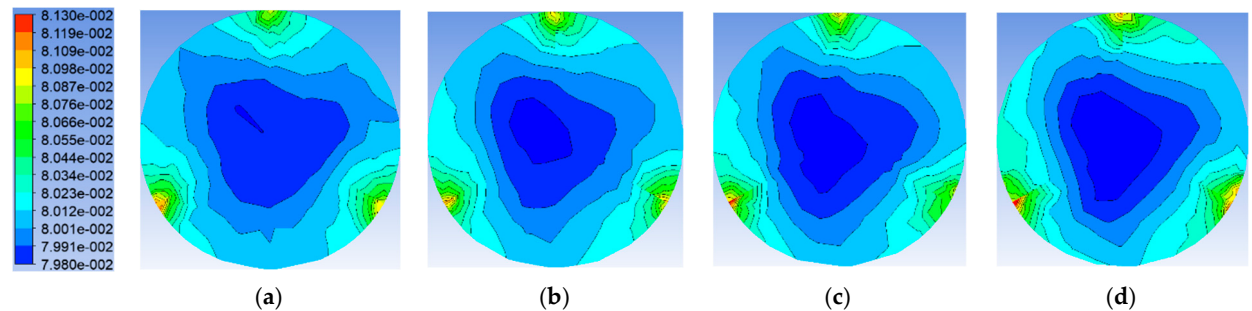


Figure 14. Effect of the placement angle of twist tape near datum plane of  $Z = 30 D$  on the distribution of hydrate particle concentration. (a)  $\theta = 10^\circ$ . (b)  $\theta = 15^\circ$ . (c)  $\theta = 20^\circ$ . (d)  $\theta = 25^\circ$ .

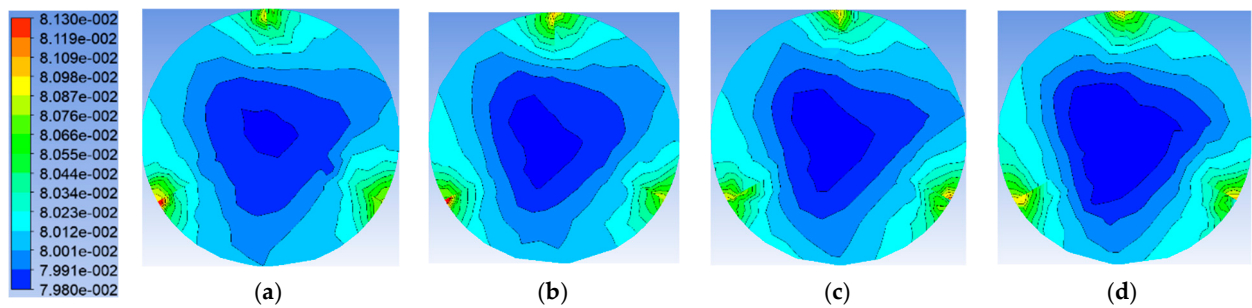


Figure 15. Effect of the placement angle of twist tape near datum plane of  $Z = 50 D$  on the distribution of hydrate particle concentration. (a)  $\theta = 10^\circ$ . (b)  $\theta = 15^\circ$ . (c)  $\theta = 20^\circ$ . (d)  $\theta = 25^\circ$ .

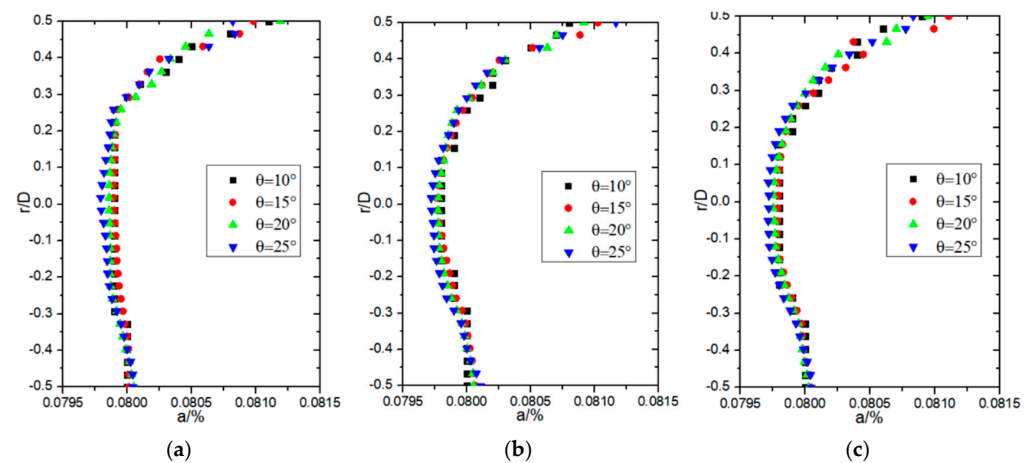
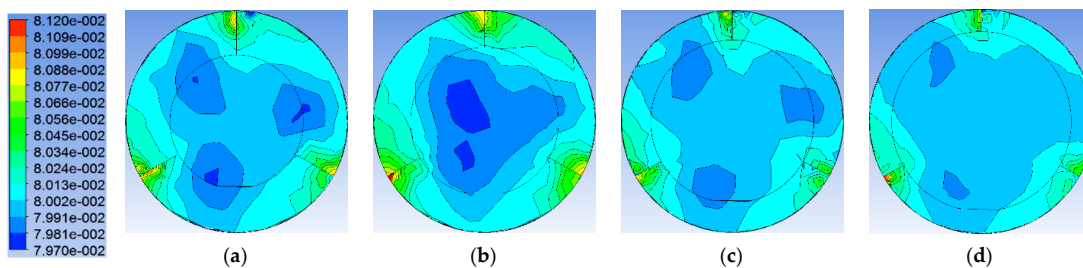


Figure 16. Influence of placing angle of twist tape near different datum planes on vertical distribution of hydrate particle concentration. (a)  $Z = 10 D$ . (b)  $Z = 30 D$ . (c)  $Z = 50 D$ .

From Figure 16, it can be seen that the concentration at the bottom of the pipe is basically unchanged, there is no deposition phenomenon, and the concentration near the twist tape at the top of the pipe is the highest. From the numerical value of particle concentration, it can be seen that different placement angles have no obvious influence on the maximum concentration near the twist tape. This shows that the particles only flow together near the twist tape and do not accumulate and deposit or stick to the twist tape.

### 3.3.2. Influence of the Height of Twist Tape on the Distribution Law of Particle Volume Fraction

Figures 17–19 show the flow twist tape height versus hydrate particle concentration at  $Z = 8 D$ ,  $30 D$ , and  $47 D$  sections under the condition of  $Re = 20,000$ . From the distribution diagram, it can be seen that the high-concentration areas of particles are concentrated near the three twist tapes, the concentration of particles on the leeward side of the twist tape is higher than that on the windward side, and the minimum concentration area at the axis position gradually becomes larger with the increase of the flow distance. It shows that the swirl has a good particle carrying effect, and the particles will not be deposited in the center of the tube bottom due to the influence of gravity. Comparing the hydrate accumulation areas near the four twist tapes of different heights, it can be found that for the flow bar pipeline from  $h = D/10$  to  $h = D/6$ , the particle accumulation area increases with the increase of the height of the twist tape, and a quarter of the blank section appears at the upper end of the twist tape with  $h = D/5$ . This shows that under the premise of the same swirl flow intensity, the range of particle aggregation area has a constant value, which will not increase indefinitely with the increase of the length of the twist tape. Figure 20 shows the influence of the height of flow twist tapes at different cross sections on the radial distribution of hydrate particle concentration under the working condition of  $Re = 20,000$ . The abscissa is the concentration, and the ordinate is the ratio of the distance between the detection point and the pipe axis and pipe diameter. It can be seen from the figure that the concentration at the bottom of the pipe is basically unchanged and there is no deposition phenomenon. The concentration near the twist tape at the upper end of the pipe is the highest. From the numerical value of particle concentration, it can be observed that the axial concentration of the twist tape with  $h = D/6$  is the lowest, indicating that the swirl flow of particles in the pipe with  $h = D/6$  has the best particle carrying effect.



**Figure 17.** Influence of the height of twist tape on hydrate particle concentration distribution at  $Z = 8 D$  section. (a)  $h = D/5$ . (b)  $h = D/6$ . (c)  $h = D/8$ . (d)  $h = D/10$ .

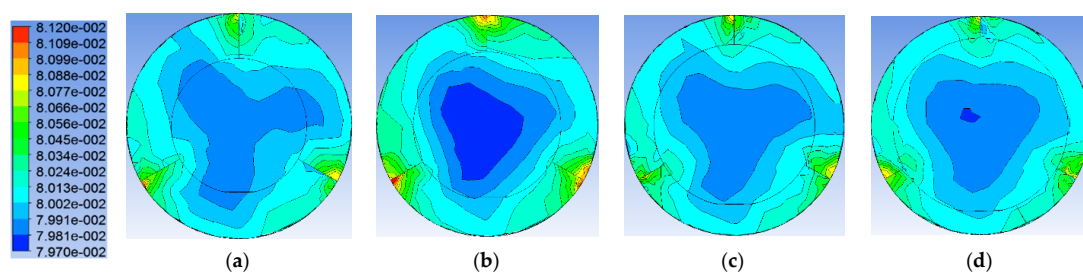


**Figure 18.** Influence of the height of twist tape on hydrate particle concentration distribution at  $Z = 30 D$  section. (a)  $h = D/5$ . (b)  $h = D/6$ . (c)  $h = D/8$ . (d)  $h = D/10$ .



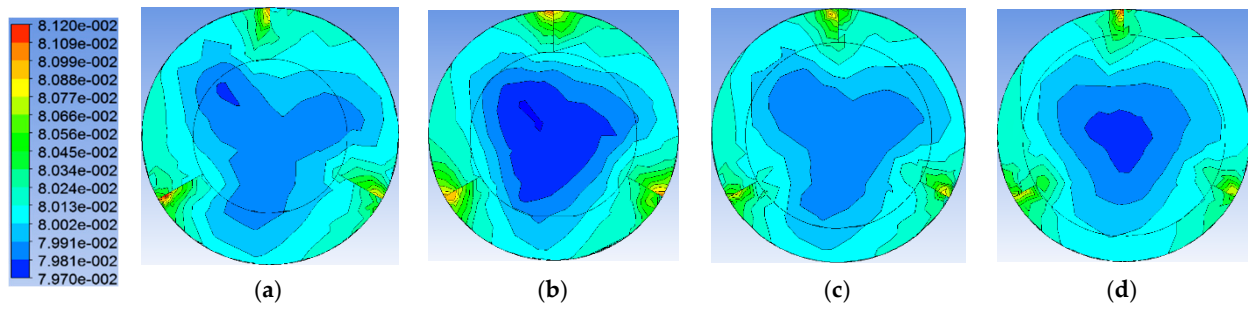


**Figure 19.** Influence of the height of twist tape on hydrate particle concentration distribution at  $Z = 47 D$  section. (a)  $h = D/5$ . (b)  $h = D/6$ . (c)  $h = D/8$ . (d)  $h = D/10$ .

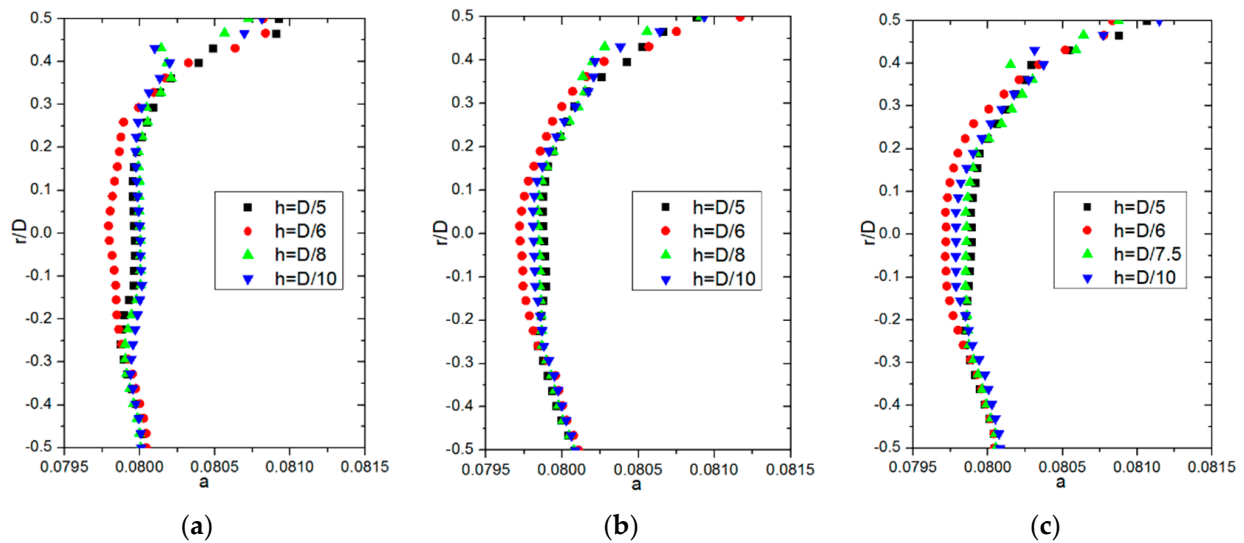


**Figure 20.** Influence of the height of flow twist tape on the radial distribution of hydrate particle concentration at different vertical sections. (a)  $Z = 8 D$ . (b)  $Z = 30 D$ . (c)  $Z = 47 D$ .

### 3.3.3. Influence of the Number of Twist Tapes on the Distribution Law of Particle Volume Fraction

Figures 21 and 22 show the relationship between the number of flow twist tapes and hydrate particle concentration at  $Z = 14 D$  and  $42 D$  sections under the condition of  $Re = 20,000$ . From the distribution diagram, it can be seen that the high-concentration areas of particles are concentrated near three twist tapes, the concentration of particles on the leeward side of the twist tape is higher than that on the windward side, and the minimum concentration area at the axis position gradually becomes larger with the increase of the flow distance. It shows that the swirl has a good particle carrying effect, and the particles will not be deposited in the center of the tube bottom due to the influence of gravity. By comparing the hydrate accumulation areas near three different twist tapes, it can be found that the hydrate particles in the twist tape with  $n = 4$  gather the most, while the twist tape with  $n = 6$  has no obvious dark area in the interval shown in the legend. This is because the swirl number of the twist tape with  $n = 6$  is too low, the spacing between twist tapes is too small, and the effective flow area on the cross section of the pipe is too low, resulting in no obvious concentration difference between the leeward side of the twist tape and the windward side of the next twist tape. It shows that the number of twist tapes should not be too much, which will affect the carrying effect of swirl flow.

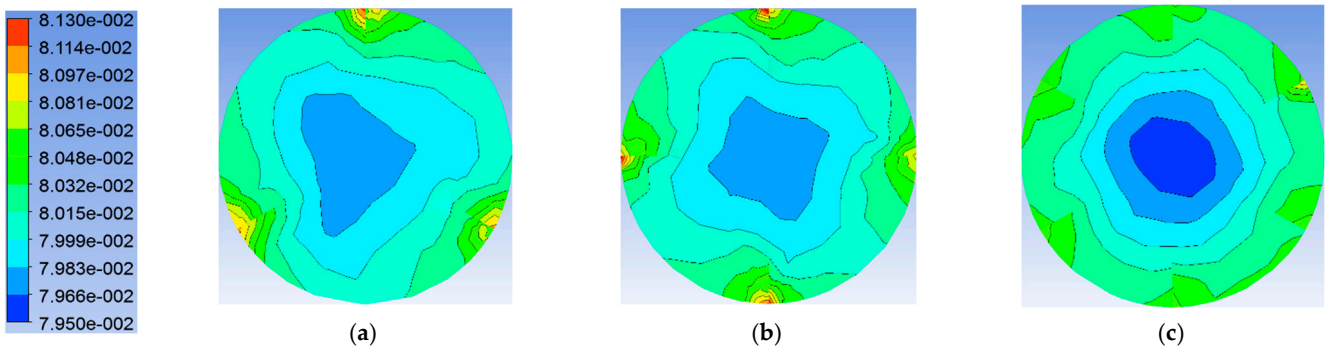


**Figure 21.** Influence of the number of flow twist tapes on hydrate particle concentration distribution at  $Z = 14 D$  section. (a)  $n = 3$ . (b)  $n = 4$ . (c)  $n = 6$ .

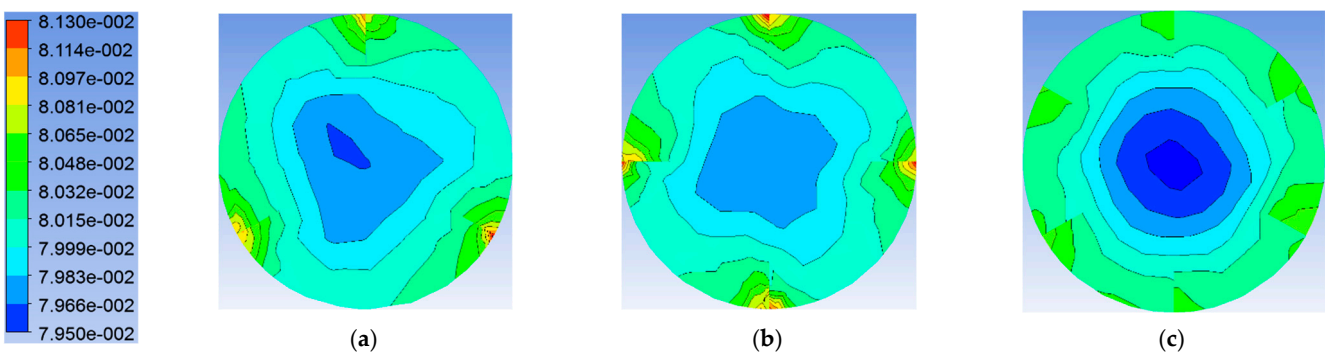


**Figure 22.** Influence of the number of twist tapes on hydrate particle concentration distribution at  $z = 42 D$  section. (a)  $n = 3$ . (b)  $n = 4$ . (c)  $n = 6$ .

Shown in Figures 23 and 24 is the concentration of flow twist tape to hydrate particles at different particle concentrations under the condition of  $Re = 20,000$ . From the influence diagram, it can be seen that with the increase of the initial particle concentration, the particle aggregation position is still near the twist tape, and it does not accumulate and deposit at the bottom of the pipe. In practical application, the particle concentration will not be higher than 50%, so it can be concluded that the particles in the flow guide pipe will not deposit at the bottom of the pipe at the high Reynolds number of  $Re = 20,000$ .

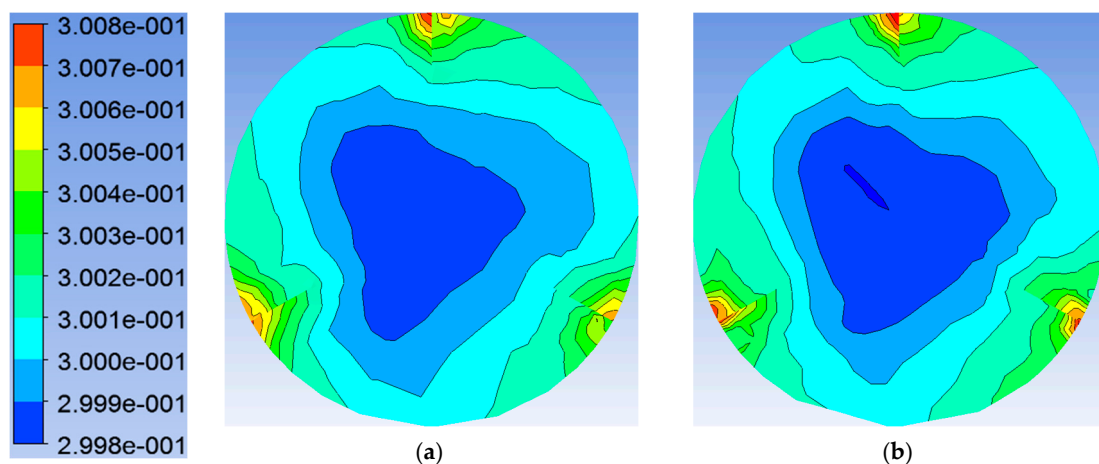


**Figure 23.** Influence of flow twist tape on the distribution of hydrate particle concentration at the initial particle concentration of 30%. (a)  $Z = 14 D$ . (b)  $Z = 42 D$ .

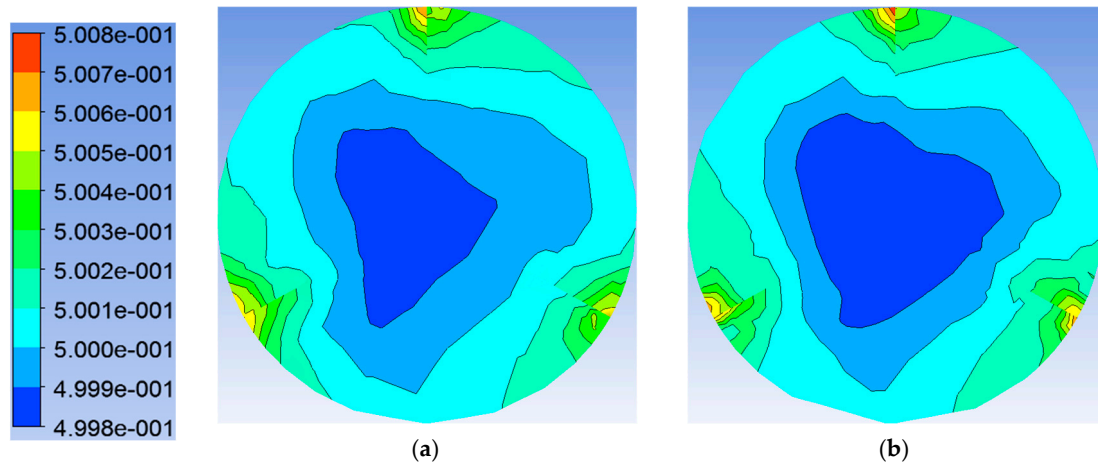


**Figure 24.** Influence of flow twist tape on the distribution of hydrate particle concentration at the initial particle concentration of 50%. (a)  $Z = 14 D$ . (b)  $Z = 42 D$ .

As shown in Figure 25, the flow twist tape–hydrate particle concentration at different initial particle concentrations in the 23 D section at Reynolds number  $Re = 5000$  is shown. In the influence diagram, it can be seen that with the increase of initial particle concentration, the particle concentration near the twist tape directly above the pipe gradually decreases, and at the initial particle concentration  $\alpha_0 = 20\%$ , the particle concentration of the upper twist tape is close to the initial particle concentration.

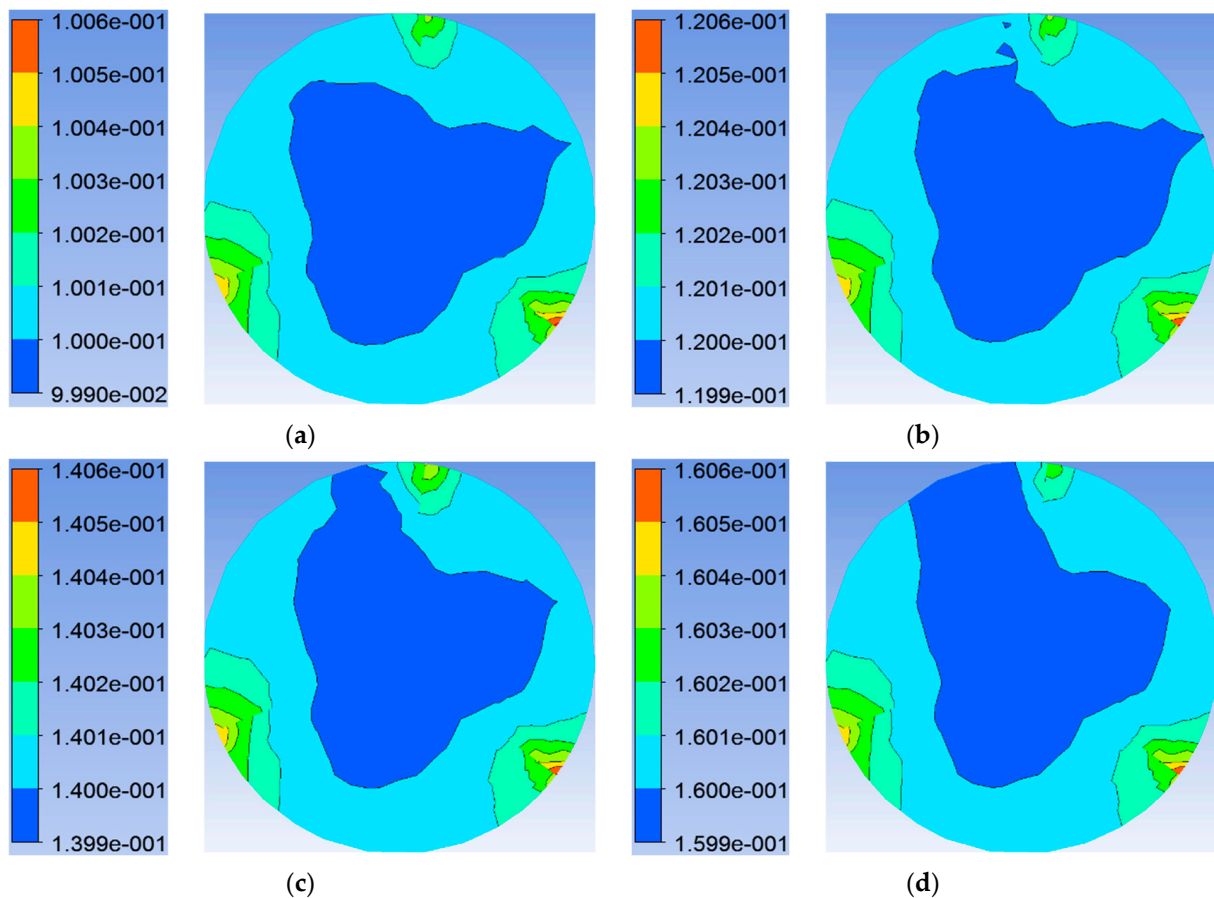


**Figure 25.** Cont.

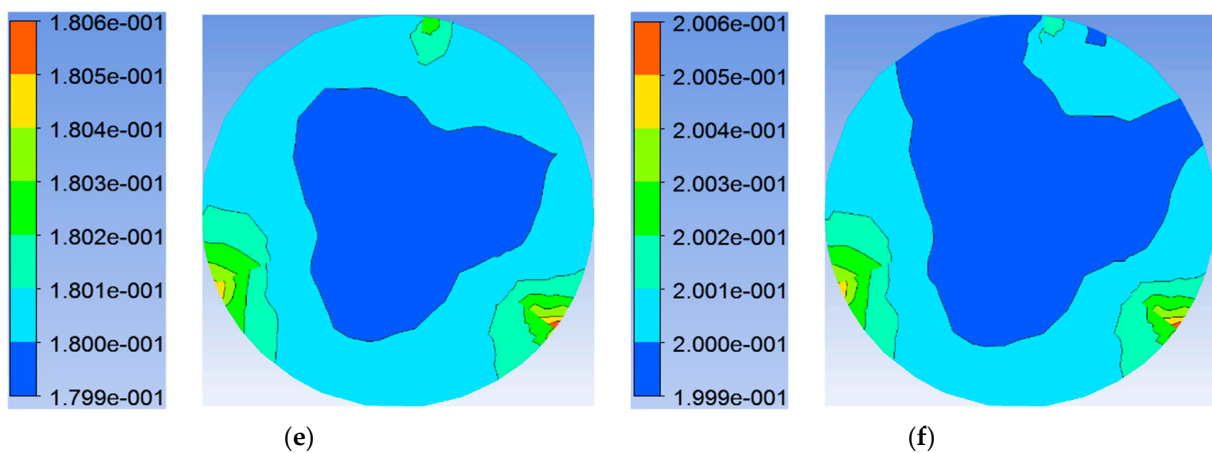


**Figure 25.** Influence of flow twist tape on hydrate particle concentration distribution under different initial particle concentrations. (a)  $\alpha_0 = 10\%$ . (b)  $\alpha_0 = 12\%$ . (c)  $\alpha_0 = 14\%$ . (d)  $\alpha_0 = 16\%$ . (e)  $\alpha_0 = 18\%$ . (f)  $\alpha_0 = 20\%$ .

Because the fluid will generate vertical lift under the action of the twist tape and the vertical lift will increase the twist degree of the fluid streamline at the windward side of the twist tape, a swirl flow with stable velocity circulation and uniform vortex strength can be formed in the pipeline. The increase of particle concentration destroys this stable mechanism, which makes the swirl flow insufficient to carry all the particles for complete annular flow. It can be roughly judged from the figure that under the condition of a low Reynolds number of  $Re = 5000$ , there is an extreme value of particle concentration carried by the swirl flow, and the maximum particle concentration carried by the swirl flow = 14%.

### 3.4. Optimization of Structural Parameters of Twist Tape

In order to better judge the placement angle of twist tape, the evaluation parameters of the swirl efficiency of a gas–solid two-phase pipeline are introduced. Physically, in order to determine the placement, one must calculate the number of swirling flows produced by the pressure drop per unit length. The formula is defined as:

$$\xi = \frac{\bar{S}}{\Delta P/l} \quad (12)$$

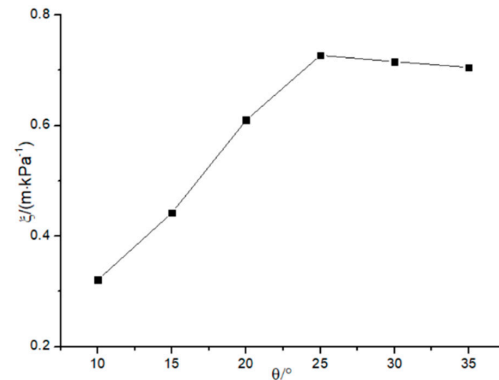
where the  $\xi$  of the unit is  $m/kPa$ ;  $\bar{S}$  is the average swirl number in the tube, which is obtained by averaging the data on the vertical section and the horizontal section, and  $\Delta P/l$  is the pressure drop per unit length in  $kPa/m$ .

#### 3.4.1. Optimization of Setting Angle of Twist Tape

Table 2 and Figure 26 show different setting angles, respectively, evaluation parameters of the swirl efficiency of a gas–solid two-phase pipeline with twist tapes, and calculation results and graphs. The setting angle can be seen from Table 2 and Figure 26. The parameter is larger, and the angle of placement is greater. For every 5-degree increase in the range of 10~25, one must add 0.12 to the parameter and place it at the angle  $\theta$ . The maximum value is reached when it is 25 degrees. When the setting angle is greater than 25 degrees, the parameter began to decrease slowly, indicating that the excessive setting angle at this time led to the excessive resistance of the flow twist tape to the fluid. Therefore, from the perspective of economic benefits, the placement angle  $\theta = 25^\circ$ , and it is the best setting angle of the twist tape.

**Table 2.** Calculation result of evaluation parameters of swirl efficiency of gas–solid two-phase pipeline with twist tape.

	$\theta=10^\circ$	$\theta=15^\circ$	$\theta=20^\circ$	$\theta=25^\circ$	$\theta=30^\circ$	$\theta=35^\circ$
$\bar{S}$	0.016487	0.024929	0.037083	0.045768	0.052309	0.059673
$\Delta P/l$	0.051364	0.056354	0.060808	0.065710	0.073082	0.084617
$\xi$	0.320988	0.442354	0.609838	0.726954	0.715758	0.705213

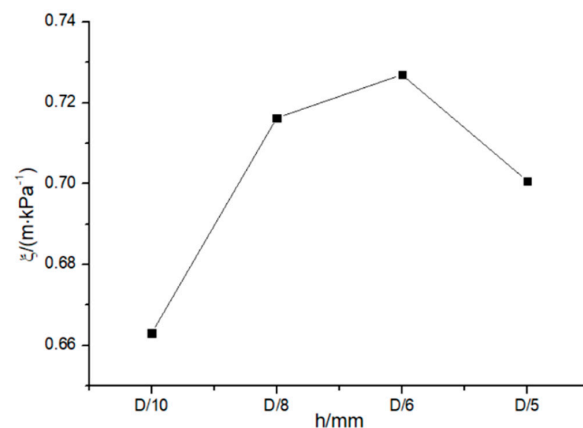
**Figure 26.** Calculation results graph of swirl efficiency of gas–solid two-phase pipeline with different placement angles.

### 3.4.2. Height Optimization of Twist Tape

Table 3 and Figure 27 show the swirl efficiency evaluation parameters of a gas–solid two-phase pipeline with twist tapes of different heights, respectively. From the calculation results and graphs, it can be seen from Table 3 and Figure 27 that with the increase of height, the evaluation parameters increase first and then decrease in a parabolic shape, and when  $h = D/6$ , the coefficient reaches a peak. When  $h = D/5$ , although the swirl number and pressure drop are both increasing, the greater increase of pressure drop leads to excessive resistance of the twist tape to the fluid, so its coefficient decreases. Therefore, considering the economic benefits,  $h = D/6$  is the best height of the diversion pipe.

**Table 3.** Calculating results of the pipeline swirling efficiency evaluation parameter of gas–solid two-phase pipeline with different heights.

	$H = D/5$	$H = D/6$	$H = D/8$	$H = D/10$
$\bar{S}$	0.04965	0.047768	0.04452	0.036036
$\Delta P/l$	0.0708583	0.0657098	0.062157	0.0543459
$\xi$	0.700695	0.726954	0.716246	0.663077

**Figure 27.** Calculation result curve of pipeline swirling efficiency evaluation parameter of gas–solid two-phase pipeline with different heights.



### 3.4.3. Optimization of the Number of Twist Tapes

Table 4 and Figure 28 show the swirl efficiency evaluation parameters of a gas–solid two-phase pipeline with twist tapes of different heights, respectively. From calculation results and graphs, it can be seen from Table 4 and Figure 28 that with the increase of the number, the evaluation parameters increase first and then decrease, reaching a peak when  $n = 3$ . When  $n = 2$ , although the unit pressure drop is the lowest, the average swirl number is lower, so the coefficient is a minimum value. When  $n = 4$  and 6, the unit pressure drop is large due to the low number of swirling flows, and the resistance of the twist tape to the fluid is too great, so its coefficient decreases. Therefore, considering the economic benefits, the optimal number of twist tapes is three.

**Table 4.** Calculating results of the pipeline swirling efficiency evaluation parameter of gas–solid two-phase pipeline with different numbers.

	$n = 2$	$n = 3$	$n = 4$	$n = 6$
$\bar{S}$	0.041112	0.049555	0.048231	0.046615
$\Delta P/l$	0.064697	0.0657098	0.0662719	0.06783
$\xi$	0.635455	0.754148	0.727775	0.687222

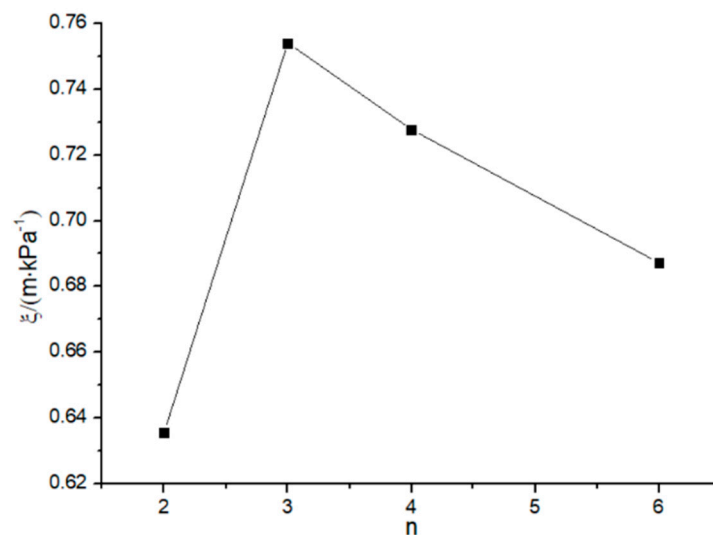


**Figure 28.** Calculation result curve of pipeline swirling efficiency evaluation parameter of gas–solid two-phase pipeline with different numbers.

### 3.5. Comparison and Analysis of Whole-Process Twist Tape, Local Twist Taping, and Common Pipelines

Using the Fluent software, numerical simulation was carried out for the whole-process rotation of the twist tape, the local rotation of the twist tape, the local rotation of the twist tape, and the common pipeline, respectively. By comparing and analyzing the simulation results, the improvement of hydrate transportation efficiency of the whole-process rotation of the twist tape, compared with other methods, can be obtained.

#### 3.5.1. Comparison of Attenuation Law of Swirl Number by Different Twist Tape Methods

Figure 29 shows the influence of different whirling devices on the number of whirls along the way under the working condition of  $Re = 5000$ . It can be seen from the figure that the number of whirls along the way with local whirling will be attenuated when the fluid exits the end of the whirling device. The initial number of whirls of the twist tape with local whirling is larger than that of the twist tape, and the attenuation of the number of whirls is slower than that of the twist tape with local whirling, indicating that the local whirling efficiency of the twist tape is higher than that of the twist tape. However, when the twist

tape rotates all the way, the swirl number curve of the twist tape fluctuates sinusoidally after reaching the initial swirl number, and the swirl number will not be attenuated. Therefore, when  $Z = 0.43$  m, the number of the local swirl of the twist tape is equal to that of the twist tape. When the flow distance is greater than 0.43 m, the number of the local swirl of the twist tape is clearly larger than that of the twist tape. This shows that the efficiency of the whole-process twist tape of the twist tape in the pipeline with a total length of 2 m is about 4.65 times that of the local twist tape of the four-leaf twist tape. In the same way, the efficiency of the whole rotation of the twist tape is about 12.5 times that of the local rotation of the twist tape. Because the swirl flow will not appear in the horizontal smooth tube without the twist tape, the swirl number is zero in the whole tube section.

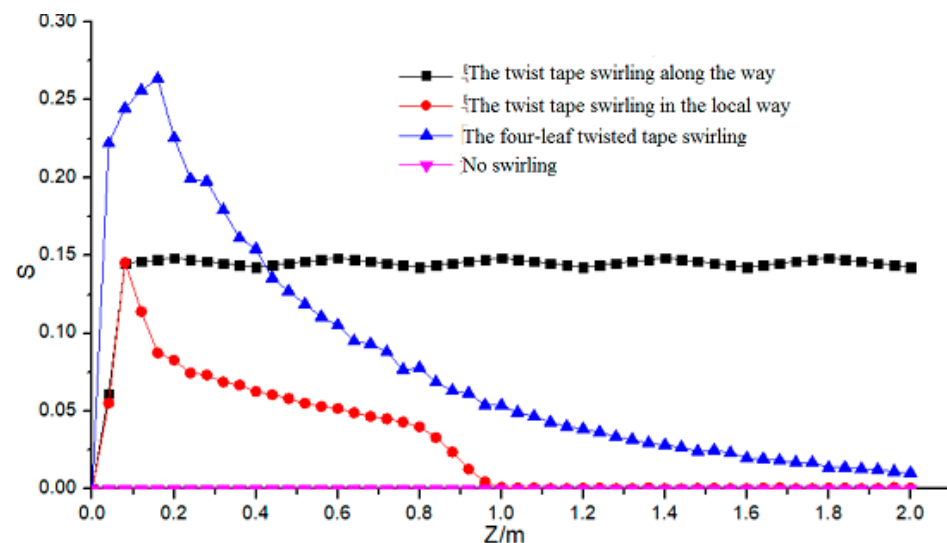
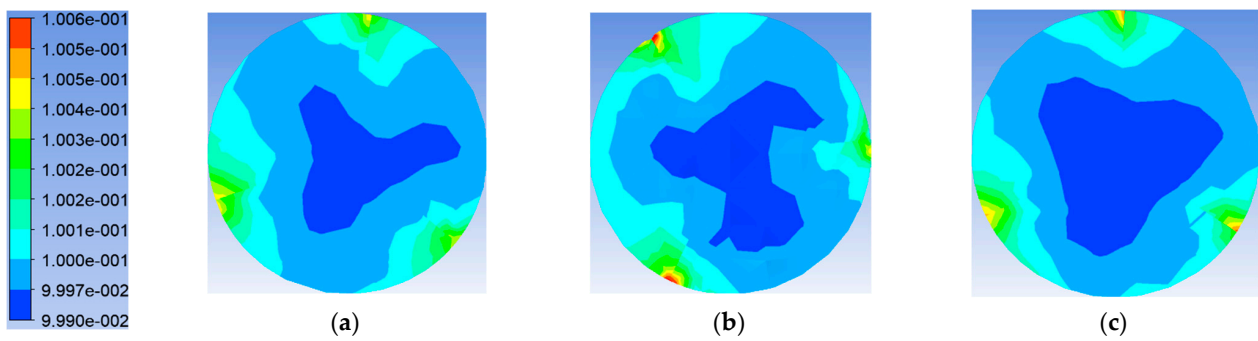


Figure 29. Influence of different twist tapes on the swirl number along the way.

### 3.5.2. Comparison of Distribution Rules of Particle Volume Fraction by Different Twist Tapes

Figures 30–33, respectively, show the particle concentration distribution of different sections under the condition of  $Re = 5000$ , with the twist tape rotating all the way, with the twist tape rotating locally, with the twist tape rotating locally, and with an ordinary pipeline. At  $Re = 5000$ , hydrate particle size is 10  $\mu\text{m}$ , and the initial particle concentration is 10%. It can be seen from Figure 30 that, in the pipeline with the twist tape rotating all the way, the particles gather near the twist tape, and the axis position is a low-concentration area. Except when the twist tape passes through the bottom of the pipe, there is no high-concentration area at the bottom of the pipe, so the particles do not deposit. As shown in Figure 31, due to the rapid attenuation of swirl number, the particles are more obviously affected by gravity, and the particle concentration begins to stratify from top to bottom at 10 D. With the increase of flow distance, the swirl number further attenuates, and the particle concentration at the bottom of the pipe gradually increases. However, as shown in Figure 32, in the twist tape local twist tape pipeline, the local twist tape effect of the twist tape is better than that of the twist tape, and the initial swirl number generated by the twist tape local twist tape pipeline is much larger than that of the twist tape. Therefore, the hydrate particles at the 10 D section of the twist tape local twist tape pipeline are dispersed outwards by centrifugal force and evenly distributed near the pipe wall. With the increase of flow distance, the amount of swirling flow decreases continuously; the gravity effect of particles becomes obvious gradually, and particles begin to deposit at the bottom of the pipe. As shown in Figure 33, in ordinary pipelines, because there is no tangential stress, particles gradually deposit at the entrance of the pipeline.



**Figure 30.** Distribution diagram of particle concentration at different sections of the whole-process rotating pipe of the twist tape. (a)  $Z = 10 D$ . (b)  $Z = 30 D$ . (c)  $Z = 50 D$ .

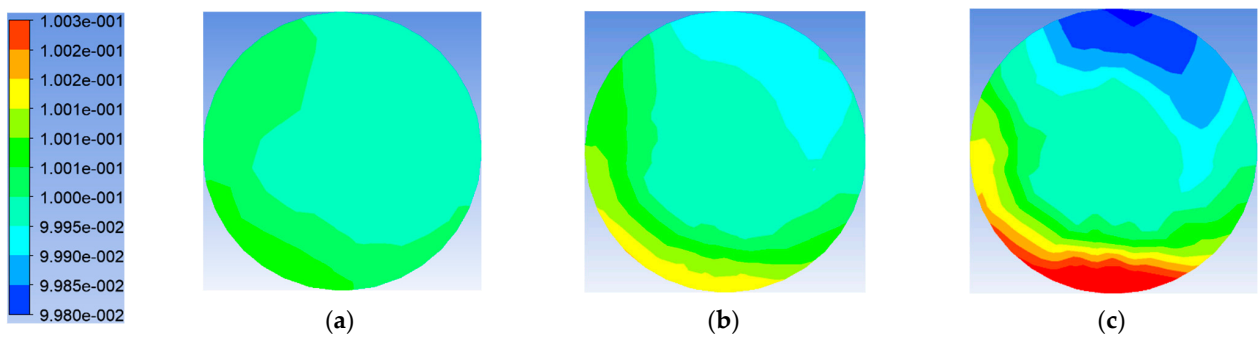


**Figure 31.** Distribution diagram of particle concentration at different sections of local rotating pipe of twist tape. (a)  $Z = 10 D$ . (b)  $Z = 30 D$ . (c)  $Z = 50 D$ .

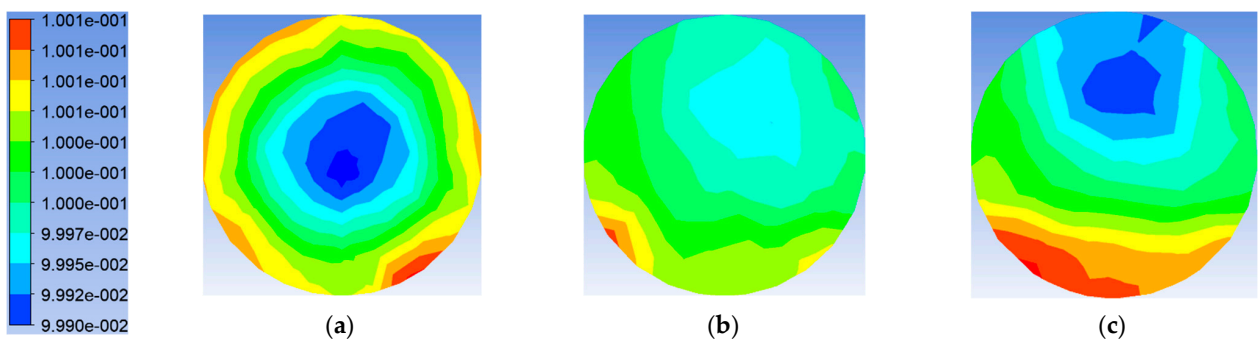


**Figure 32.** Distribution diagram of particle concentration at different cross sections in the local twist tape pipe of the twist tape. (a)  $Z = 10 D$ . (b)  $Z = 30 D$ . (c)  $Z = 50 D$ .

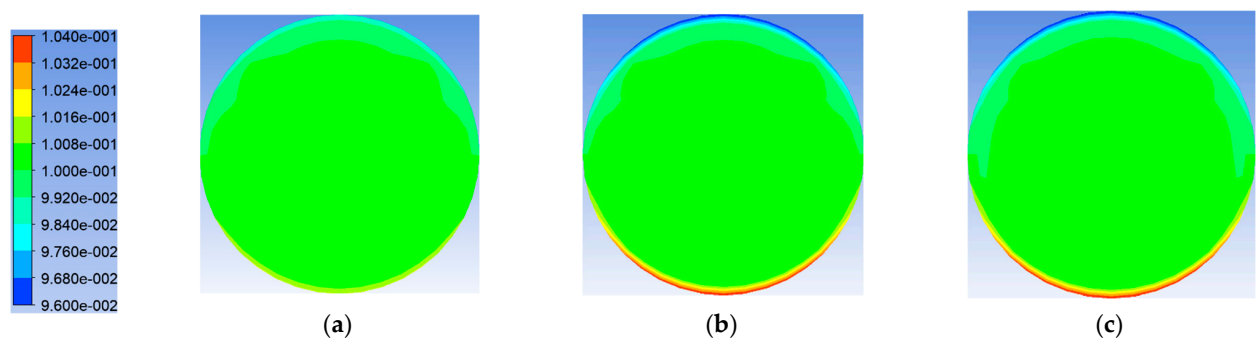


**Figure 33.** Distribution diagram of particle concentration at different cross sections of the smooth pipe without twist tape. (a)  $Z = 10 D$ . (b)  $Z = 30 D$ . (c)  $Z = 50 D$ .

Particles will be continuously deposited in the pipeline due to gravity, and the deposited particles may be blown up again. If they are not blown up, they will accumulate, and the thickness of the particle layer will become higher and higher, which is referred to as particle deposition. The critical deposition position refers to the position where the particles just begin to deposit. Figures 34–37 are the nephograms of the variation of particle concentration with time at the cross section of the critical deposition position of particles under different twist tapes. We set  $Re = 5000$ , particle size  $D_k = 10 \mu\text{m}$ , and initial particle concentration  $\alpha_0 = 10\%$ . In the simulation, three time periods were selected, namely,  $t = 0.2 \text{ s}$ ,  $t = 0.4 \text{ s}$ , and  $t = 0.8 \text{ s}$ . The critical deposition position of hydrate particles was estimated by observing the change of particle deposition on the cross section of the pipeline. Figure 34 shows the sediment cloud image of particles changing with time at the cross section of  $Z = 66 \text{ D}$  in the whole rotating pipeline of the twist tape. It can be seen from Figure 34 that the particle concentration on the cross section of the pipeline is basically unchanged with the increase of time, indicating that the particles do not deposit in the pipeline. Since  $Z = 66 \text{ D}$  is close to the outlet of the pipeline, it can be considered that there is no critical deposition position of particles in the pipeline under the condition that the flow twist tape rotates all the way; that is, hydrate particles do not deposit at the bottom of the pipeline. As shown in Figure 35, the sediment cloud chart of particles on the cross section of the twist tape with local rotation  $Z = 20 \text{ D}$  changes with time. In Figure 35, it can be seen that particles are deposited at the bottom of the pipe by gravity, its layer thickness gradually increases with time, and the particle concentration in the lower half of the pipe is higher than that in the upper half of the pipe. Figure 36 shows the sediment cloud picture of particles changing with time on the cross section of  $Z = 35 \text{ D}$  of a twist tape pipeline. In the figure, the thickness of particle layer increases with time, and the deposition range of particles in the local swirl tube is more concentrated than that of the twist tape. Figure 37 shows the sediment cloud image of particles in the section of ordinary pipeline with  $Z = 10 \text{ D}$ . At  $Z = 10 \text{ D}$ , the thickness of the hydrate particle layer at the bottom of the pipeline increases obviously with time, which indicates that particles begin to deposit at this position, and the deposition becomes more and more obvious with time. Comparing the deposition positions of four kinds of pipelines, it can be found that the particle carrying distance of the local rotating pipe of the twist tape is about 2 times higher than that of the ordinary pipeline, that of the twisted pipe is 3.5 times higher than that of the ordinary pipeline, and that of the whole rotating pipe of the twist tape is 6.6 times higher than that of the ordinary pipeline. Compared with the twisted pipe, the particle carrying effect is increased by 89%, 230%, and 560%. Therefore, the whole rotation of the twist tape can effectively increase the transportation distance of hydrate particles and provide a guarantee for the safety of the pipeline.

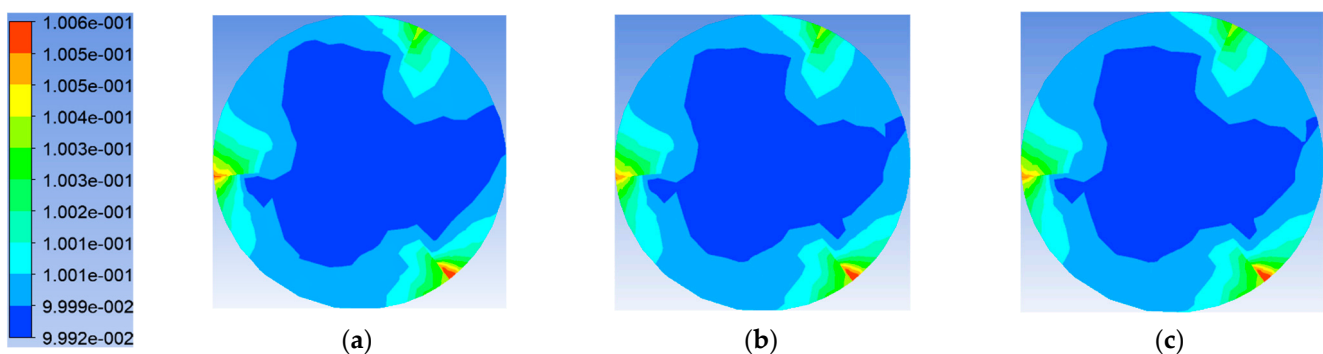


**Figure 34.** Deposition cloud chart of particles in the whole rotating pipeline of twist tape with time change. (a)  $t = 0.2 \text{ s}$ . (b)  $t = 0.4 \text{ s}$ . (c)  $t = 0.8 \text{ s}$ .

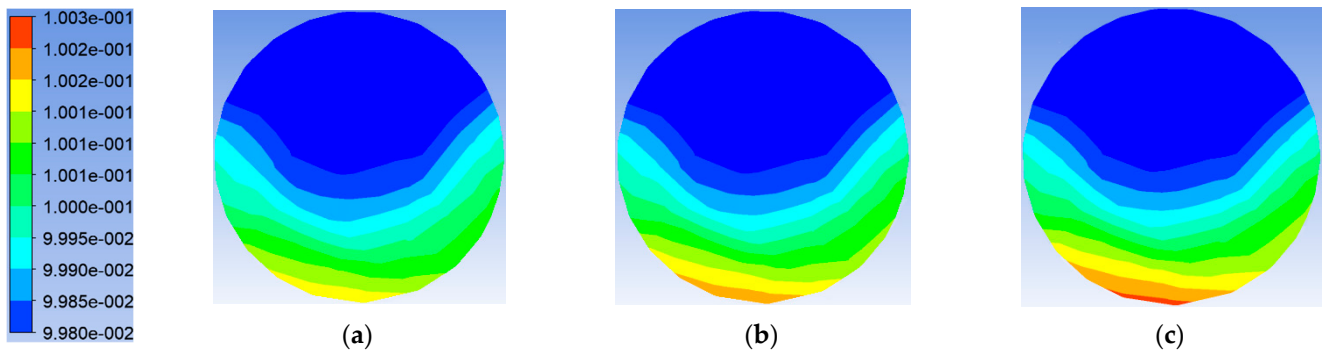


**Figure 35.** Deposition cloud chart of local swirling pipeline particles of twist tape with time change. (a)  $t = 0.2$  s. (b)  $t = 0.4$  s. (c)  $t = 0.8$  s.

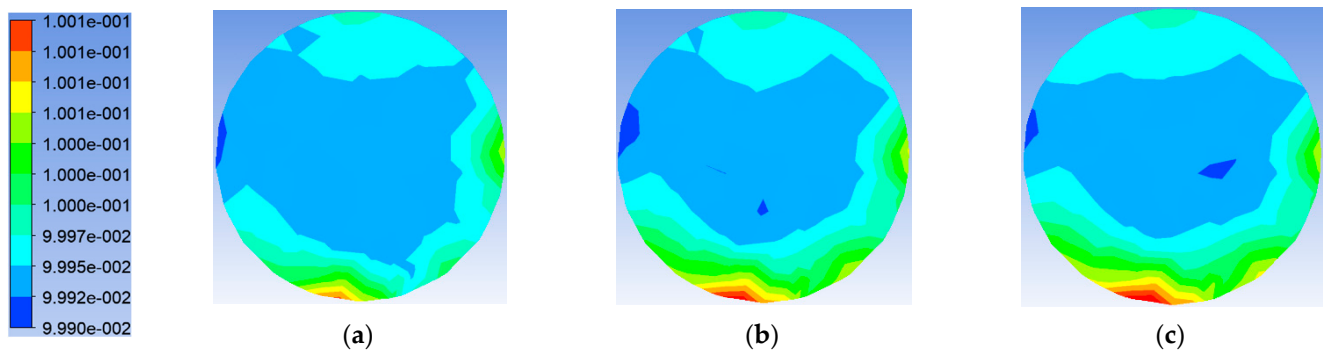


**Figure 36.** Deposition cloud chart of local swirling pipeline particles with twist tape. (a)  $t = 0.2$  s. (b)  $t = 0.4$  s. (c)  $t = 0.8$  s.

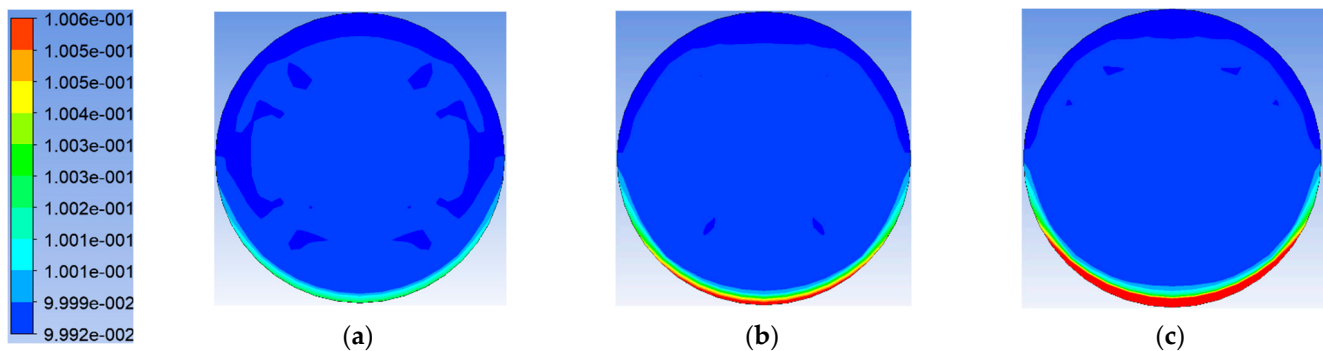


**Figure 37.** Sedimentary cloud diagram of time-varying particles in the smooth pipe without twist tape. (a)  $t = 0.2$  s. (b)  $t = 0.4$  s. (c)  $t = 0.8$  s.

#### 4. Conclusions

(1) The maximum radial swirl number appears in the range of  $0.4\text{--}0.45 D$ , and the swirl number at the axis of the pipeline tends towards 0. The swirl number in the tube is rotationally symmetrical around the center of the circle by  $360^\circ$ , and it increases first and then decreases periodically from the windward side of the twist tape to the leeward side of the next twist tape. The diversion angle is greater, and the maximum swirl number is greater. The diversion height is higher, and the attenuation of radial swirl number is slower. The number of twist tapes is higher, and the number of swirl flows between the two plates is lower. The curve of the stationary section of rotation is sinusoidal. The angle of the twist tape is greater; the deviation and amplitude of the curve is greater, and the fluctuation frequency is faster. The height of the guide is higher, and the deviation of its curve is greater. The twist tapes are greater in number, and the curve offset is greater.



(2) The high-concentration areas of particles are concentrated near the three twist tapes, and the concentration of particles on the leeward side of the twist tapes is higher than that on the windward side. The minimum concentration area at the axial position gradually becomes larger with the increase of the flow distance, and hydrate particles do not deposit at the bottom of the whole pipe section. The placement angle of the twist tape is greater, and the high-concentration area of particles near the twist tape is larger. Under the condition of constant swirl strength, the range of high particle concentration area will not increase indefinitely, and it will be constant. The range of the high particle concentration area will be invariable when the height of the twist tape is  $D/6$ . The number of twist tapes should not be too great, as this will affect the particle carrying effect.

(3) The evaluation parameters of the swirl efficiency of a gas–solid two-phase pipeline are proposed. These parameters represent the swirl efficiency of twist tapes. The optimal setting angle of twist tapes is 25 degrees; the optimal height is  $D/6$ , and the optimal number of twist tapes is 3.

(4) The number of swirling flow along the local vortex will be attenuated when the fluid exits the end of the vortex device. There is no swirling flow in the common pipeline, and the amount of swirling flow is zero in the whole pipeline section. In a pipeline with a total length of 2 m, the efficiency of the whole-process rotation of the twist tape is about 4.65 times that of the local rotation of the 4-leaf twist tape, and the efficiency of the whole-process rotation of the twist tape is about 12.5 times that of the local rotation of the twist tape.

(5) The particle carrying distance of the local swirl flow generation is about two times higher than that of the ordinary pipe. The particle carrying distance of the 4-twist tape pipe is 3.5 times higher than that of the ordinary pipe. The particle carrying distance of the whole swirl flow generation is 6.6 times higher than that of the ordinary pipe. The particle carrying effect is 89% higher than that of the 4-twist tape pipe. The particle carrying effect is 230% higher than that of the local swirl flow generation. The particle carrying effect is 560% higher than that of the ordinary pipe.

**Author Contributions:** Conceptualization, S.W. and C.H.; methodology, J.Y.; software, S.W.; validation, S.W., Y.R. and S.Z.; formal analysis, C.H.; investigation, J.Y.; resources, S.W.; data curation, S.W.; writing—original draft preparation, S.W.; writing—review and editing, Y.R. and S.Z.; visualization, S.W. and C.H.; supervision, J.Y.; project administration, S.W.; funding acquisition, S.W. All authors have read and agreed to the published version of the manuscript.

**Funding:** This work was supported by Open Project of Collaborative Innovation Center for Clean Energy Application Technology (Quanzhou Vocational and Technical University) (No. QJNY22-06, QJNY22-01, and QJNY22-04), Quanzhou Science and Technology Planning Project (No.2022N045), the National Nature Science Foundation of China (No.51574045 & 51974037), the CNPC Innovation Foundation (No.2020D-5007-0211), the Project of Emission Peak and Carbon Neutrality of Jiangsu Province, China (No. BE2022001-5), and the General Project of Natural Science Research in Jiangsu Universities (No.22KJB440002).

**Data Availability Statement:** Data are contained within this article.

**Acknowledgments:** This work was supported by Jiangsu Key Laboratory of Oil and Gas Storage and Transportation Technology.

**Conflicts of Interest:** The authors declare no conflict of interest.

## Nomenclature

$C_D$	drag coefficient
$C_{1\epsilon}, C_{2\epsilon}$	turbulence model coefficient
$d_p$	particle diameter [m]
$G_k, G_b$	turbulent kinetic energy
$g_z$	component of gravity acceleration in the z direction [ $m/s^2$ ]
$P$	static pressure, [Pa]
$Re$	relative Reynolds number

$T$	time [s]
$u_p$	particle velocity [m/s]
$u, v, w$	speed [m/s]
$\rho$	gas density [kg/m <sup>3</sup> ]
$\rho_p$	particle density [kg/m <sup>3</sup> ]
$\tau_{ij}$	viscous stress tensor
$\sigma_k, \sigma_\epsilon$	turbulent Platt number of $k$ and $\epsilon$

## References

- Zhang, S. *Study on Accident Risk Analysis and Route Selection Method of Long-Distance Oil and Gas Pipeline*; China University of Mining and Technology: Beijing, China, 2012.
- Minbo, W.; Junjie, Q.; Weiqing, C. Towards the development of cavitation technology for gas hydrate prevention. *R. Soc. Open Sci.* **2021**, *8*, 202054.
- Esterhuyse, S.; Sokolic, F.; Redelinghuys, N.; Avenant, M.; Kijko, A.; Glazewski, J.; Plit, L.; Kemp, M.; Smit, A.; Vos, A.T.; et al. Vulnerability mapping as a tool to manage the environmental impacts of oil and gas extraction. *R. Soc. Open Sci.* **2017**, *4*, 171044. [[CrossRef](#)] [[PubMed](#)]
- Austfrik, T.; Loken, K.P. Deposition of CO<sub>2</sub> on the seabed in the form of hydrates. *Energy Convers Manag.* **1992**, *33*, 659–666. [[CrossRef](#)]
- Gudmundsson, J.S. Cold flow hydrate technology. In Proceedings of the Fourth International Conference on Gas Hydrate, Yokohama, Japan, 19–23 May 2002; Tapir Academic Press: Yokohama, Japan, 2002; pp. 912–916.
- Andersson, V.; Gudmundsson, J.S. Transporting oil and gas as hydrate slurries. *BHR Group Hydrotransp.* **1999**, *14*, 181–191.
- Wang, S.L.; Rao, Y.C.; Zhou, S.D. Experimental study on natural gas pipeline transportation by hydrate method. *Nat. Gas Ind.* **2014**, *34*, 101–107.
- Wang, S.L.; Rao, Y.C.; Wu, Y.X. Experimental study on gas-liquid swirl flow with twist tape. *Hydrodyn. Res. Prog.* **2013**, *28*, 105–110.
- Rao, Y.C.; Wang, S.L.; Dai, W.J.; Zheng, Y.X.; Liu, Z.Y.; Jiang, Y.H. Research progress on rheology and safe flow boundary of natural gas hydrate slurry. *Chem. Eng. Prog.* **2015**, *34*, 3551–3556.
- Zhou, Y.L.; Zhang, L.Y. Numerical Simulation of Gas-Liquid Two-Phase Flow Pattern Conversion in a Rectangular Section of a Swirl Pipe. *Chem. Ind. Eng.* **2014**, *65*, 4767–4774.
- Wang, S.L.; Rao, Y.C.; Wu, Y.X. Experimental study on gas-liquid two-phase swirl flow in horizontal pipe. *J. Exper. Mech.* **2013**, *28*, 77–86.
- Dai, Y.; Rao, Y.C.; Wang, S.L. Experimental study on gas-liquid two-phase swirl flow in horizontal tube under degradable surfactant system. *Exper. Mech.* **2014**, *31*, 134–140.
- Cai, B.; Xia, G.D.; Yang, G. Study on Flow Pattern and Pressure Drop Characteristics of Gas-Liquid Two-Phase Flow in Screw Channel. *J. Eng. Therm.* **2016**, *37*, 1690–4774.
- Liu, X.F.; Xia, G.D.; Yang, G. Experimental study on the slug flow in a swirl channel with rectangular cross section. *J. Chem. Ind. Eng.* **2016**, *7*, 1690–4774.
- Liu, S.L.; Cai, W.H.; Li, F.C. Numerical Simulation of Flow Pattern and Heat Transfer Characteristics of Vapor-Liquid Two-Phase Flow in horizontal Pipe. *J. Eng. Therm.* **2014**, *46*, 57–64.
- Cui, W.Z.; Li, L.J.; Xin, M.D. An experimental study of flow pattern and pressure drop for flow boiling inside microfinned helically coiled be. *Int. J. Heat Mass Transf.* **2018**, *51*, 169–175. [[CrossRef](#)]
- Subhashini, V.; Nigam, K.D.P. Experimental investigation of void fraction and flow patterns in coiled flow inverter. *Chem. Eng. Process.* **2008**, *47*, 1281–1291.
- Liu, X.F.; Xia, G.D.; Yang, G. Experimental study on the characteristics of air–water two-phase flow in vertical helical rectangular channel. *Int. J. Multiph. Flow* **2015**, *73*, 227–237. [[CrossRef](#)]
- Fabio, T.K.; Gherhardt, R. Two-phase flow patterns and pressure drop inside horizontal tubes containing twisted-tape inserts. *Int. J. Multiph. Flow* **2012**, *47*, 50–65.
- Wang, S.; Ding, B.; Rao, Y.; Chen, F. Study on the influence of coconut oil on flow pattern and pressure drop of two-phase swirl flow. *RSC Adv.* **2019**, *9*, 32644–32655. [[CrossRef](#)]
- Wang, S.L.; Rao, Y.C.; Wu, Y.X.; Wang, X.B. Experimental research on gasliquid two-phase swirl flow in horizontal pipe. *Pet. Process. Petrochem. Technol.* **2012**, *14*, 24–32.
- Wang, S.L.; Rao, Y.C.; Wei, M.J.; Zhang, L.; Ma, W.J. Experimental study on pressure drop of gas-liquid two-phase swirl flow in horizontal tube. *Sci. Technol. Eng.* **2013**, *13*, 659–663.
- Li, J.M.; Wang, S.L.; Rao, Y.C.; Zhao, S.H.; Zhang, Y.F.; Wang, L. Effect of Surfactants on Flow Characteristics of Gas-Liquid Two-Phase Swirl Tube Flow. *J. Hydrodyn.* **2015**, *1*, 18–23.
- Liu, W.; Lv, X.F.; Bai, B.F. Axial development of air–water annular flow with swirl in a vertical pipe. *Int. J. Multiph. Flow* **2020**, *124*, 103165. [[CrossRef](#)]
- Liu, W.; Lv, X.F.; Bai, B.F. The effect of swirl on transition from churn flow to annular flow in an intermediate diameter pipe. *Exp. Therm. Fluid Sci.* **2019**, *109*, 109861. [[CrossRef](#)]

26. Liu, W.; Luo, Z.-y.; Bai, B.-f. Characteristics of swirl vortex induced by swirl ties in pipes. *J. Chem. Eng.* **2011**, *62*, 3115–3122.
27. Cai, Y.Y.; Li, B.B.; Rao, Y.C.; Wang, S.L.; Ge, H.; Yan, S.; Liang, J. Numerical simulation of flow characteristics of hydrate slurry with long twist tape. *Pet. Mach.* **2018**, *46*, 106–113+119.
28. Liang, J.; Rao, Y.C.; Wang, S.L.; Li, L.J.; Sun, Q. Numerical simulation of swirl flow and heat transfer in hydrate pipeline with impeller rotation. *Pet. Mach.* **2018**, *46*, 120–126.
29. Hu, X.Y.; Gao, L.; Li, Z.W. Experimental study on swirl flow characteristics of pipes containing polyacrylamide. *Adv. Water Resour. Hydropower Sci. Technol.* **2019**, *39*, 19–26.
30. Rao, Y.C.; Li, L.J.; Wang, S.L.; Zhao, S.H.; Zhou, S.D. Numerical Simulation Study on Flow Laws and Heat Transfer of Gas Hydrate in the Swirl Flow Pipeline with Long Twisted Band. *Entropy* **2021**, *23*, 489. [[CrossRef](#)]
31. Rao, Y.; Liu, Z.; Wang, S.; Li, L.; Sun, Q. Numerical Simulation of Swirl Flow Characteristics of CO<sub>2</sub> Hydrate Slurry by Short Twisted Band. *Entropy* **2021**, *23*, 913. [[CrossRef](#)]
32. Monfared, R.H.; Niknejadi, M.; Toghraie, D.; Barnoon, P. Numerical investigation of swirling flow and heat transfer of a nanofluid in a tube with helical ribs using a two-phase model. *J. Therm. Anal. Calorim.* **2022**, *147*, 3403–3416. [[CrossRef](#)]
33. Miansari, M.; Darvishi, M.R.; Toghraie, D.; Barnoon, P.; Shirzad, M.; Alizadeh, A. Numerical investigation of grooves effects on the thermal performance of helically grooved shell and coil tube heat exchanger. *J. Chem. Eng.* **2022**, *44*, 424–434. [[CrossRef](#)]
34. Rao, Y.; Wang, S.; Li, L. Numerical Simulation of the Flow Pattern of Spiral Annular Flow with a Guide Strip by Spiral On-Way. *ACS Omega* **2022**, *7*, 31961–31973. [[CrossRef](#)] [[PubMed](#)]
35. Ko, M.-S.; Chang, T.-B.; Lee, C.-Y.; Huang, J.-W.; Lim, C.-F. Optimization of Cyclone-Type Rotary Kiln Reactor for Carbonation of BOF Slag. *Sustainability* **2021**, *13*, 11556. [[CrossRef](#)]
36. Chang, T.-B.; Lee, C.-Y.; Ko, M.-S.; Lim, C.-F. CFD simulations of rotary BOF slag carbonation kiln reactor with cyclone flow. *Proc. Inst. Mech. Eng. Part E J. Process Mech. Eng.* **2019**, *234*, 37–45. [[CrossRef](#)]
37. Zhou, J.W.; Liu, Y.; Du, C.L.; Liu, S.Y. Effect of the particle shape and swirling intensity on the breakage of lump coal particle in pneumatic conveying. *Powder Technol.* **2017**, *317*, 438–448. [[CrossRef](#)]

**Disclaimer/Publisher’s Note:** The statements, opinions and data contained in all publications are solely those of the individual author(s) and contributor(s) and not of MDPI and/or the editor(s). MDPI and/or the editor(s) disclaim responsibility for any injury to people or property resulting from any ideas, methods, instructions or products referred to in the content.